

NAVAL POSTGRADUATE SCHOOL MONTEREY, CALIFORNIA



THESIS

BATHYMETRY FROM HYPERSPECTRAL IMAGRY

by

L. Douglas Stuffle

December, 1996

Thesis Advisor:

R. C. Olsen

Co-Advisor:

Newell Garfield

Approved for public release; distribution is unlimited.

DTIC QUALITY INSPECTED 3

19970925 027

REPORT DOCUMENTATION PAGE			Form Approved OMB No. 0704-0188	
Public reporting burden for this collection of information is estimated to average 1 hour per response, including the time for reviewing instruction, searching existing data sources, gathering and maintaining the data needed, and completing and reviewing the collection of information. Send comments regarding this burden estimate or any other aspect of this collection of information, including suggestions for reducing this burden, to Washington Headquarters Services, Directorate for Information Operations and Reports, 1215 Jefferson Davis Highway, Suite 1204, Arlington, VA 22202-4302, and to the Office of Management and Budget, Paperwork Reduction Project (0704-0188) Washington DC 20503.				
1. AGENCY USE ONLY (Leave blank)	2. REPORT DATE December, 1996.	3. REPORT TYPE AND DATES COVERED Master's Thesis		
4. BATHYMETRY FROM HYPERSPECTRAL IMAGRY		5. FUNDING NUMBERS		
6. AUTHOR(S) L. Douglas Stuffle.				
7. PERFORMING ORGANIZATION NAME(S) AND ADDRESS(ES) Naval Postgraduate School Monterey CA 93943-5000		8. PERFORMING ORGANIZATION REPORT NUMBER		
9. SPONSORING/MONITORING AGENCY NAME(S) AND ADDRESS(ES)		10. SPONSORING/MONITORING AGENCY REPORT NUMBER		
11. SUPPLEMENTARY NOTES The views expressed in this thesis are those of the author and do not reflect the official policy or position of the Department of Defense or the U.S. Government.				
12a. DISTRIBUTION/AVAILABILITY STATEMENT Approved for public release; distribution is unlimited.			12b. DISTRIBUTION CODE	
13. ABSTRACT (maximum 200 words) This work used hyperspectral imagery to derive shallow water depth estimates. A technique to classify substrates and estimate reflectance values for the substrate types is the major contributions of this work. This was accomplished by masking different bottom types based on spectra, effects that were not included in previous methods. HYDICE data was taken over Lake Tahoe on June 22, 1995. The high altitude of the lake provided a low aerosol content within the atmosphere. This allowed for relatively straight forward atmospheric corrections. This was substantially easier than in an oceanic environment. The atmospheric radiative transfer code MODTRAN3.0 was used to model the atmospheric conditions at the time of the experiment. The radiative transfer code HYDROLIGHT3.5 was used to model the attenuation coefficients of the relatively clear water of the lake. Minimal river input and low chlorophyll concentrations made it simpler to determine these values. Making use of the full spectral content of data within the optical range, multiple substrates were differentiated and masked off. This allowed for an estimation on wet substrate reflectance and a straight forward calculation of bottom depth.				
14. SUBJECT TERMS: Hyperspectral, Visible, Imagery, Bathymetry, HYDICE, MODTRAN3.5, HYDROLIGHT3.0,			15. NUMBER OF PAGES 87	
			16. PRICE CODE	
17. SECURITY CLASSIFICATION OF REPORT Unclassified	18. SECURITY CLASSIFICATION OF THIS PAGE Unclassified	19. SECURITY CLASSIFICATION OF ABSTRACT Unclassified	20. LIMITATION OF ABSTRACT UL	

Approved for public release; distribution is unlimited.

BATHYMETRY FROM HYPERSPECTRAL IMAGRY

L. Douglas Stuffle
Lieutenant, United States Navy
B. S., University of Arizona, 1990

Submitted in partial fulfillment
of the requirements for the degree of

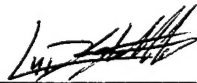
MASTER OF SCIENCE IN PHYSICS

from the

NAVAL POSTGRADUATE SCHOOL

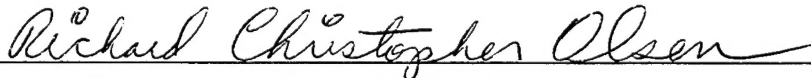
December, 1996

Author:

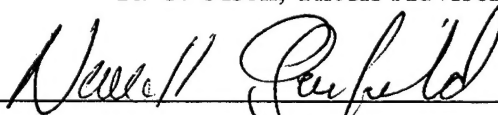


L. Douglas Stuffle

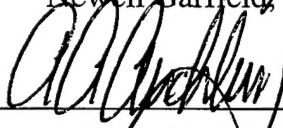
Approved by:



R. C. Olsen, Thesis Advisor



Newell Garfield, Co-Advisor



Anthony A. Atchley, Chairman
Department of Physics

ABSTRACT

This work used hyperspectral imagery to derive shallow water depth estimates. A technique to classify substrates and estimate reflectance values for the substrate types is the major contributions of this work. This was accomplished by masking different bottom types based on spectra, effects that were not included in previous methods. HYDICE data was taken over Lake Tahoe on June 22, 1995. The high altitude of the lake provided a low aerosol content within the atmosphere. This allowed for relatively straight forward atmospheric corrections. This was substantially easier than in an oceanic environment. The atmospheric radiative transfer code MODTRAN3.0 was used to model the atmospheric conditions at the time of the experiment. The radiative transfer code HYDROLIGHT3.5 was used to model the attenuation coefficients of the relatively clear water of the lake. Minimal river input and low chlorophyll concentrations made it simpler to determine these values. Making use of the full spectral content of data within the optical range, multiple substrates were differentiated and masked off. This allowed for an estimation on wet substrate reflectance and a straight forward calculation of bottom depth.

TABLE OF CONTENTS

I. INTRODUCTION	1
II. BATHYMETRY	3
A. WEIGHTED LINE SOUNDINGS.....	3
B. SONAR SOUNDINGS	5
C. DEPTH MEASUREMENTS WITH LIDAR.....	6
D. ALTIMETER DEPTH MEASUREMENTS.....	7
E. PASSIVE OPTICAL METHODS.....	9
1. Satellite Spectral Remote Sensing	9
2. Airborne Spectral Remote Sensing	11
3. Recent Developments	13
III. OPTICAL MEASUREMENTS	15
A. GEOMETRICAL RADIOMETRY.....	15
1. Radiance.....	15
2. Irradiance	16
3. Reflectance.....	16
4. Radiance Invariance.....	17
B. LIGHT AND HOW IT INTERACTS WITH WATER.....	18
1. Inherent Optical Properties	19
a. <i>Spectral Absorptance</i>	20
b. <i>Spectral Scatterance</i>	20
c. <i>Spectral Transmittance</i>	21
d. <i>Other Significant Quantities</i>	21
2. Water Constituents.....	22
3. Summing the Different Inherent Optical Properties	23
4. Absorption in Water.....	23
a. <i>Absorption in Pure Water</i>	24
b. <i>Absorption Due to Dissolved Organic Matter</i>	26
c. <i>Absorption Due to Phytoplankton and Organic Detritus</i>	26
d. <i>Contributions From Sediment</i>	27
e. <i>Deriving a Model for Total Absorption</i>	27
5. Scattering in Water	28
C. RADIATIVE TRANSFER.....	29
1. Radiative Transfer at the Water	31
D. BATHYMETRY FROM REMOTELY SENSED RADIATION.....	32
1. Unmixing Effects Due to Depth and Substrate Reflectance - The Bierwirth Algorithm - An Exploitation of LANDSAT Data	32
2. Empirical Model - Hamilton Algorithm - An Application of AVIRIS Data	35

IV. MEASUREMENTS AT LAKE TAHOE	37
A. MEASUREMENTS AT LAKE TAHOE.....	37
B. INSTRUMENTS	37
V. INITIAL MODEL APPLICATION.....	39
A. APPLICATION OF THE BIERWIRTH METHOD TO LAKE TAHOE DATA..	40
1. Processed HYDICE Data	40
2. Atmospheric Contributions	42
<i>a. Path Radiance</i>	<i>43</i>
<i>b. Sky Radiance</i>	<i>43</i>
<i>c. Convolving Modtran3.5 Data to Match HYDICE.....</i>	<i>44</i>
<i>d. Water Leaving Radiance.....</i>	<i>46</i>
<i>e. Normalizing to Reflectance</i>	<i>47</i>
3. Depth Derivation.....	48
<i>a. HYDROLIGHT, a Radiative Transfer Model</i>	<i>49</i>
<i>b. Results of Bierwirth</i>	<i>50</i>
B. APPLICATION OF THE HAMILTON METHOD TO LAKE TAHOE DATA..	51
VI. DERIVING DEPTH WITH MODELED BOTTOM TYPES	53
A. MASK CONSTRUCTION	53
1. Constructing Mask for Sandy Bottom Areas	56
2. Constructing Masks for Dark Areas.....	58
3. Composite of the Bottom Types	59
B. MODELING DEPTH BY INCLUDING SUBSTRATE REFLECTANCE.....	60
1. Estimating Substrate Reflectance.....	61
<i>a. Rock Substrate</i>	<i>61</i>
<i>b. Sandy Substrate.....</i>	<i>62</i>
<i>c. Wet Substrate Reflectance.....</i>	<i>63</i>
2. Depth Results	64
<i>a. Depth by Using Bottom Reflectance Compared to Depth Without Using</i>	<i>Bottom Reflectance</i>
<i>b. Using Substrate Reflectance to Calculate Depth for Entire Scene.....</i>	<i>65</i>
C. RELIABILITY OF ATTENUATION COEFFICIENTS.....	66
VII. SUMMARY AND CONCLUSIONS	69
LIST OF REFERENCES	73
INITIAL DISTRIBUTION LIST	77

I. INTRODUCTION

A basic military need in littoral warfare is an accurate knowledge of near-shore bathymetry. This knowledge is necessary for special forces and other combatants prior to landing activities, and for marine forces traversing the coastal zone. Such "metoc" information is, of course, just one element of the intelligence information needed to plan a landing, with other elements including a knowledge of beach trafficability, and shore defenses, including mines and obstacles. The work described here addresses how bathymetric information can be obtained from (visible) spectral imagery.

Due to the complex and constantly varying nature of the interaction of electromagnetic radiation with water, it's best to begin the analysis of a new technique in a relatively benign environment. Once satisfactory results have been obtained for the model situation, one can then begin to understand the interaction within the tumultuous near-coastal regions of the ocean. Measurement taken with the hyperspectral imager HYDICE over Lake Tahoe on June 5th, 1995 provided an ideal basis to begin determining depth from hyperspectral data.

As with any measurement of spectral imagery, the data received at the sensor must be unmixed with the noise inherent within the medium through which it has traversed. For the case of measurements over water, this noise will include effects due to the atmosphere as well as the water column, both of which are extremely dynamic, changing with time and geographical position. MODTRAN3.0 is a proven radiative transfer model that has been developed over the past two decades and will be shown to provide a sufficient model for the Lake Tahoe atmosphere. In addition, the radiative transfer model HYDROLIGHT, developed by Curtis Mobley, will be used to determine the behavior of the water, or specifically, the wavelength dependent attenuation coefficients.

This thesis will take previous depth derivation algorithms and build on them to take advantage of the wealth of information available through hyperspectral imagery. It will conclude by presenting a relatively accurate depth contour of a portion of Lake Tahoe called Secret Harbor. It will begin with a brief presentation of the history of bathymetry

measurements in Chapter II followed by a discussion of the basic principles needed to understand radiative transfer and how light interacts with water in Chapter III. Chapter IV will then describe the conditions of the Lake near the time of the measurements and how those measurements were taken. Initial observation, analysis and comparison to previous algorithms is presented in Chapter V, followed by a complete discussion, in Chapter VI, of how to take advantage of the information content within the hyperspectral data as it applies to the algorithm. Finally, Chapter VII will present a discussion of the results and conclusions drawn from the modeling technique used throughout the thesis.

II. BATHYMETRY

The mapping of the Earth's oceans dates back to ancient Babylon and times when maps were constructed with chisel and rock instead of paper and pencil, or computer, Figure 2.1.



Figure 2.1. Ancient Babylonian map depicting Babylon surrounded by ocean. Gaskell (1964).

Figure 2.1 shows an ancient Babylonian map that depicts Babylon surrounded by water, somewhat as a castle is surrounded by a moat. This map and those similar to it were based on facts they could observe at the time. It wasn't until Greek mariners and others like them bravely and cautiously set out to sea that these ancient ideas on what the oceans were like, began to be disproved.

A. WEIGHTED LINE SOUNDINGS

One of the first scientific ways in which early mariners could make measurements of the ocean depth was with a weighted line, Figure 2.2.

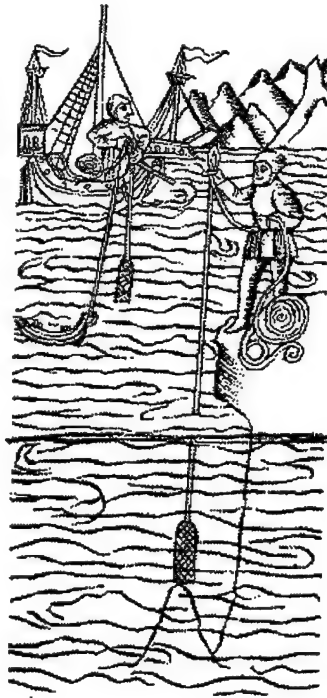


Figure 2.2. Depiction of early sounding measurements. Gaskell (1964)

This was an arduous and time consuming method. It often resulted in mediocre depth information at best, but until recent times was the only method in use.

Depth measurements are limited to how much line can be tethered from the measuring vessel. In ancient times this meant that measurements were limited to near coastal regions. As capabilities of the vessels grew, deeper measurements spanning a much larger area of the ocean were possible. As with any measuring instrument, the quality of the information produced is a function of the instrument's resolution. In the case of sounding measurements the resolution is, among other things, dependent on the quantity of the measurements, how far apart they are made and the ability of the measuring vessel to establish an accurate geographical position. In very deep water, as is normally the case in the open ocean, it sometimes takes several hours to lower and raise the sounding dredge. This makes it very difficult to take many closely spaced measurements while also maintaining an accurate position. Credit must be given, however to the crew of the British ship H.M.S. Challenger. Over the course of

Challenger's three-year expedition, the crew made a total of over two hundred soundings providing the first look at the relative transoceanic depth. The course taken by the H.M.S. Challenger is depicted in Figure 2.3 to provide the reader an idea of the scope of the effort put forth by her crew.

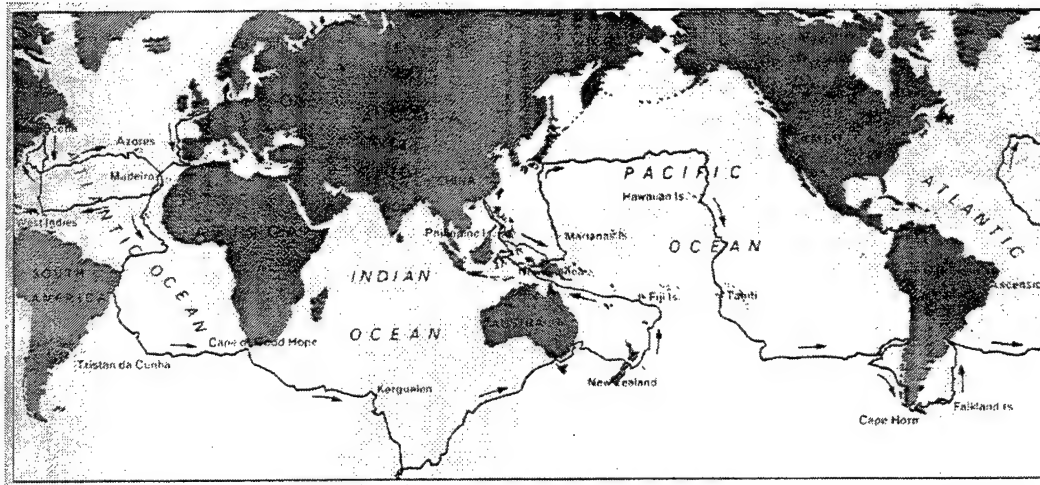


Figure 2.3. Route taken by the H.M.S. Challenger during its three year expedition to make transoceanic oceanographic measurements. Gaskell (1964).

It is interesting to note that in very near coastal water it is more accurate to use a sounding pole than a weighted line.

B. SONAR SOUNDINGS

With the advent of sonar the same measurements that used to take several hours could be made in a matter of seconds. The speed of the measurements allows for a much higher frequency of measurement along the ship's path and therefore a much better bottom resolution as shown in Figure 2.4.

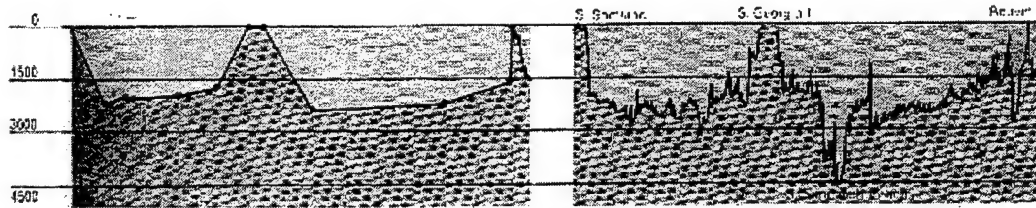


Figure 2.4. Comparison of soundings taken with weighted line (on the left) and soundings taken with sonar (on the right). Gaskell (1964).

Figure 2.4 is a comparison of weighted line soundings and sonar soundings made of the same area of the South Atlantic Ocean floor. As Gaskell (1964) points out, only 13 soundings were made with the weighted line as compared to the 1300 soundings made with sonar, resulting in a much more detailed profile.

C. DEPTH MEASUREMENTS WITH LIDAR

Just as sonar measures depth using acoustics, a Light Detection and Ranging (LIDAR) system use electromagnetic radiation to measure return time. LIDAR however, makes use of the different properties of air and water to determine the depth. It operates by sending a very short laser pulse downward from an airborne platform. Portions of the energy are reflected off the ocean surface and part is reflected off of the sea bed. The nature of the interaction between electromagnetic radiation and water will be discussed in more detail later in this paper. Given a reasonably distinct bottom return, the depth can be calculated by taking the difference between the return times of the surface and bottom reflections.

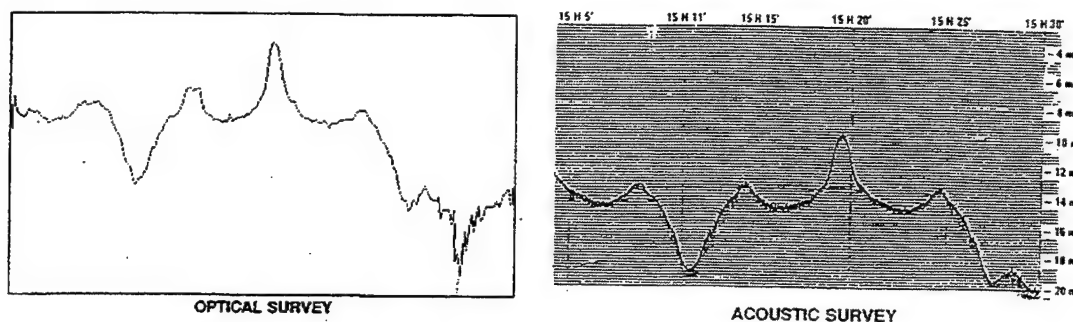


Figure 2.5. LIDAR measurements and
Acoustical measurements, Cassidy (1995)

As reported in Cassidy (1995), Figure 2.5 displays the results from a test of a French system, which shows a comparable accuracy between acoustic and optical results. Cassidy argues that a LIDAR has an advantage over acoustical methods in that it is fast, allows low cost surveys of difficult to reach or spread out coastal areas. In addition, the inherent navigational difficulties associated with coastal sonar surveys are avoided. However, it must be kept in mind that as light travels through both air and water, it experiences propagation losses that will be discussed in later chapters. This effect in fact places limitations on where and how a LIDAR system can be used.

D. ALTIMETER DEPTH MEASUREMENTS

Satellite based altimeters are capable of making depth measurements on a much wider scale than either sonar or LIDAR as can be seen in Figure 2.6. These depth measurements are the result of 4.5 years of U. S. Navy Geosat altimeter measurements and 2 years of European Remote Sensing Satellite (ERS-1) altimeter measurements. In Figure 2.6 green areas have essentially normal depth, areas with yellow-orange-red hues are relatively shallower and areas with blue-violet-magenta are increasingly deeper.

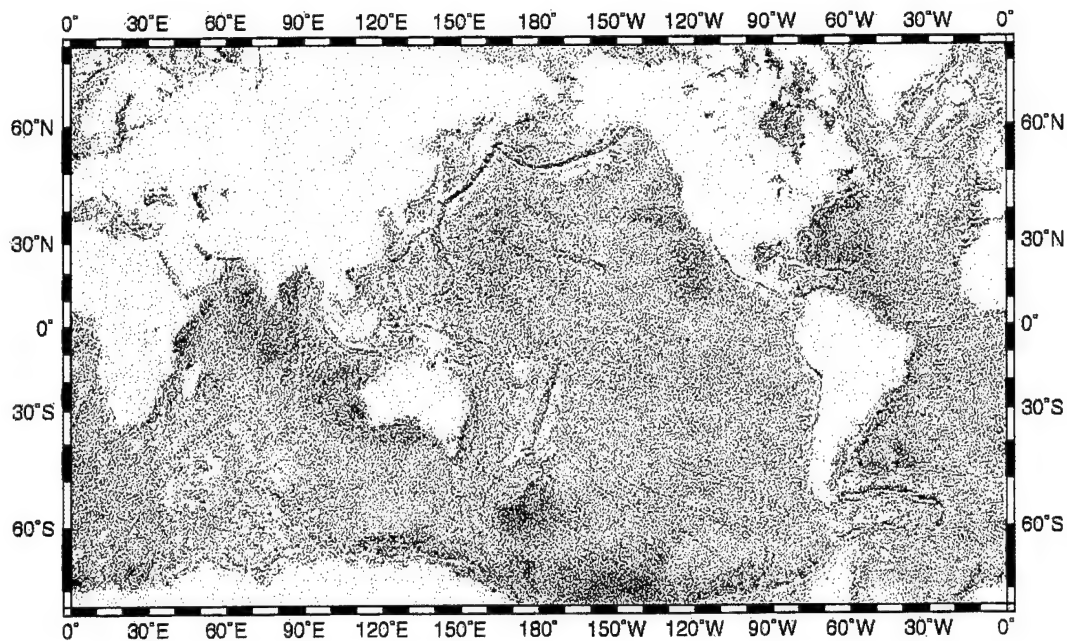


Figure 2.6. Depth derivation, on a continental scale, from altimeter measurement. From Sandwell et al. (1995).

As reported by NASA (1986), the sea surface has bulges that result from the variation in gravity in different regions of the ocean, Figure 2.7.

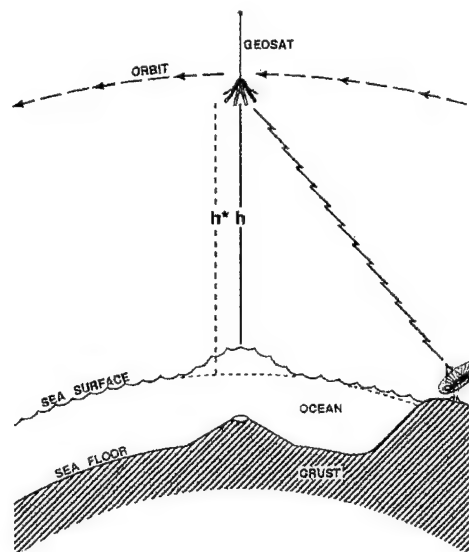


Figure 2.7. Gravitational effects on ocean surface from altimeter measurements. From Sandwell et al. (1995).

As depicted in Figure 2.7, such features as mid-oceanic ridges have a high concentration of mass and therefore will have a greater gravitational pull, causing a "pile up" of water above them. This accumulation of water can result in a rise of the sea surface as much as 5 meters. Contrary, areas where trenches exist will have less of a gravitational pull and subsequently cause a depression of the sea surface, sometimes as much as 60 meters. These variations in the sea surface can then be measured by an altimeter, using electromagnetic radiation, much as a sonar would measure depth via acoustics.

Altimeter measurements have given scientists an excellent view of the large scale depth variation within the Earth's oceans. However with resolutions on the order of 7 km, altimeter measurements are not suited for near shore bathymetry where depth variations over meter distances are needed.

E. PASSIVE OPTICAL METHODS

The field of remote sensing can be dated back to as early as 1858 when cameras were first placed on balloons and used to take large scale photographs. As outlined in Elachi (1987), this was soon followed by kites, then pigeons and eventually airplanes in 1909. Some of the earliest references that could be found with regard to depth derivation from remotely sensed data dated back to World War II, (McCurdy (1940) and Anon (1945)).

1. Satellite Spectral Remote Sensing

Spectral sensors of the type adequate for littoral or clear water bathymetry are relatively few, though the number is set to increase rapidly in the near future. The satellite sensors appropriate for this kind of work are the traditional earth resources systems, LANDSAT, CZCS (Coastal Color Zone Scanner) and SPOT (Satellite Pour l'Observation de la Terra). Making use of the visible operating range of LANDSAT,

listed in Table 2.1 (along with other operating characteristics), several papers have explored the possibilities for bathymetric depth derivations.

Table 2.1 Landsat Thematic Mapper Spectral Bands.
Derived from Collins, 1996

Band Number	Spectral Bands (μm)
1	0.45 - 0.52 (blue)
2	0.52 - 0.60 (green)
3	0.63 - 0.69 (red)
4	0.76 - 0.90 (NIR)
5	1.55 - 1.75 (SWIR)
6	10.4 - 12.5 (LWIR)
7	2.08 - 2.35 (SWIR)

In particular Lyzenga (1978) outlines a method of mapping water depth with multispectral data. Bierwirth (1993), which will be discussed in more detail later, derives an algorithm to get at sea-floor reflectance and water depth by unmixing LANDSAT imagery.

Although no references were found to bathymetric applications for SPOT, it is very capable of returning data very similar to LANDSAT. Table 2.2 list the different operating ranges of SPOT.

Table 2.2. Operating characteristics for SPOT. Information derived from Kramer (1992)

Mode of Operation	Band	Spectral Range
Multispectral	1	500 nm - 590 nm
	2	610 nm - 680 nm
	3	790 nm - 890 nm
Panchromatic	Black and White Spatial Resolution = 10 m	510 nm - 730 nm

The CZCS instrument was launched in 1978 onboard the NIMBUS-7 satellite and was the 1st multiple channel optical sensor tuned for observing the ocean environment. CZCS data was significant in that it proved that such oceanic constituents as chlorophyll and phytoplankton could be determined from remote measurements. However, given a resolution on the order of 1 km, CZCS did not prove useful for small scale or shallow water measurements.

2. Airborne Spectral Remote Sensing

The Visible / Infrared Imaging Spectrometer (AVIRIS), was one of the first airborne spectral imagers. It was developed as a result of the need for greater spectral resolution than satellite based instruments could provide and the subsequent high data volumes. The success of this sensor prompted a push to develop what is now called the hyperspectral sensor and resulted in such systems as the Hyperspectral Digital Imagery Collection Experiment sensor (HYDICE) and Advanced Airborne Hyperspectral Imaging Spectroradiometer (AAHIS). There are many other instruments currently in operation and under development that will not be discussed further here. Hyperspectral systems will shortly be included in satellite payloads; the NASA/TRW Lewis satellite is anticipated to be the first such, in 1997.

Initial results from several experiments conducted with hyperspectral sensors have been very exciting and have resulted in high quality images as shown in Figure 2.8. These data were taken on October 2nd over an area of coral reef at Kaneohe Bay, Hawaii. The scene was taken by the AAHIS instrument, operated by SETS Technology, Incorporated. AAHIS was the primary instrument flown in the Island Radiance experiment conducted by the Hyperspectral MASINT Support to Military Operations (HYMSMO) office in October, 1995 staged at Kaneohe Bay, Hawaii. Coincidentally, the figure illustrates a number of the problems in the remote sensing area. There is a substantial amount of sun glint (small white spots). The substantial color variations reflect the variety of bottom types (coral, sand, etc.), as well as water depth.

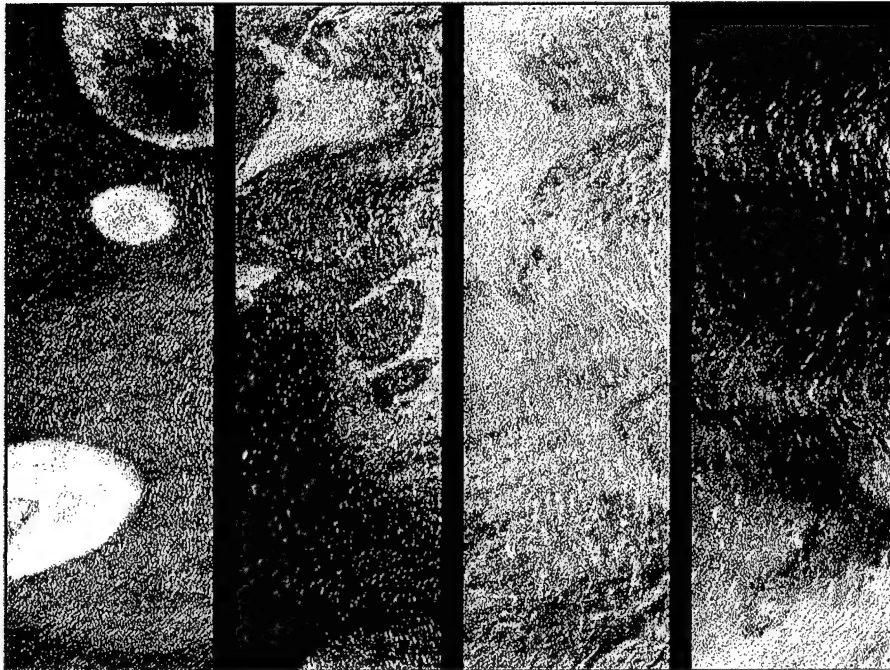


Figure 2.8. Three color image of run 2oct_r11, taken at Island radiance. Red - band 50 (705 nm), Green - band 25 (567 nm), Blue - band 1 (435 nm). Derived from data provided by HYMSMO.

Exploitation of the data for water depth was one of the primary goals of the experiment. These data offer fair possibilities, but aircraft motion makes geo-registration of the data difficult.

Several experiments have been flown over Lake Tahoe resulting in excellent data. Hamilton et al. (1993) applies an empirical model to one of these data sets in an attempt to derive depth information. The model used is based on a multiple regression of measured parameters, and requires apriori depth information; it will be discussed in greater detail later in this thesis. Table 2.3, gives the spectral operating ranges of both the HYDICE and the AVIRIS instruments.

Table 2.3. Spectral Band Characteristics of AVIRIS and HYDICE.
Derived from Collins, 1996

Instrument	Spectral Range (μm)	Number of Spectral Bands
AVIRIS	0.4 - 2.5	224
HYDICE	0.4 - 2.5	221

Kappus et al. (1996) look at Lake Tahoe data taken on June 22nd, 1995. They do not explore depth derivations, however an initial analysis of the quality and usefulness of HYDICE data in determining water radiance parameters is provided. Figure 2.9 from Kappus et al. shows that the radiance values determined from HYDICE measurements agree closely with the ground truth measurements as well as the modeled values.

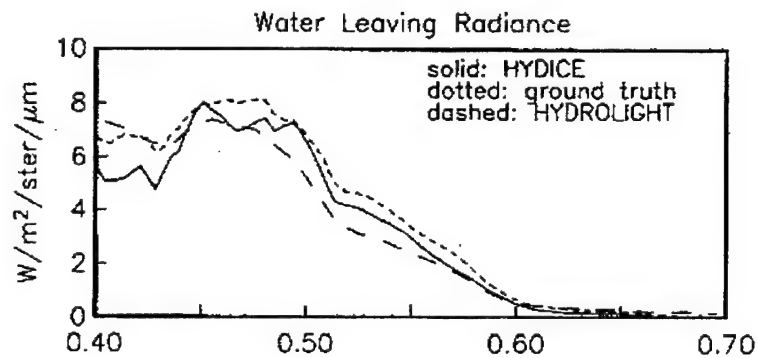


Figure 2.9. Comparison of Remotely sensed HYDICE data to that of measured and modeled data. From Kappus et al. (1996)

As will be shown later, an accurate calculation of the water leaving radiance is one of the most important steps in extracting bathymetry.

3. Recent Developments

The quality of measurements taken by CZCS prompted the development of follow-on instruments such as SeaWiFS to be carried on SeaStar and the Ocean Color and Temperature Scanner (OCTS) onboard the Advanced Earth Observing Satellite

(ADEOS). ADEOS, considered the follow on to CZCS, was launched in August 1996 and is dedicated to Earth environmental research. As described by EROC (1996), the OCTS sensor will be utilized to observe the ocean environment. Taking advantage of 12 bands covering the visible and thermal infrared regions, it measures spectral reflectance of dissolved substances, phytoplankton and sea surface temperature. These measurements will be crucial in helping researchers come to a more complete understanding of the particulate distribution within water. Understanding this distribution better, is a necessary step in deriving shallow water bathymetry. SeaWIFS is expected to gather similar information and is expected to be launched in 1997.

III. OPTICAL MEASUREMENTS

The taking of optical measurements requires an understanding of (and models for) a wide range of optical processes. Atmospheric transmittance and absorption, surface reflectance at the ocean surface, and the volumetric scattering all play important roles. In addition, when analyzing measurements over shallow waters, reflection off the substrate will play an important role as well. In the sections that follow, the optical elements needed for this study are presented.

A. GEOMETRICAL RADIOMETRY

'Spectral radiance is the fundamental radiometric quantity of interest in hydrologic optics.', Mobley (1994). It gives a foundation from where all other radiometric quantities can be derived, and provides full description of the structure of the light field, including the spatial (\bar{x}), temporal (t), directional ($\bar{\xi}$), and wavelength (λ) dependence. This is in contrast to the irradiance quantities which are measured over all directions, and therefore contain no directional dependence. Irradiance describes the target illumination while radiance defines instrument measurements.

1. Radiance

Equation [3.1] describes the quantities which comprise radiance. ΔQ is a measure of the radiant energy, within the solid angle $\Delta\Omega$, that enters a sensor and is incident upon a detector element of area ΔA within a time Δt and over a wavelength band $\Delta\lambda$.

$$L(\bar{x}; t; \bar{\xi}; \lambda) \equiv \frac{\Delta Q}{\Delta t \Delta A \Delta \Omega \Delta \lambda} \quad (\text{W m}^{-2} \text{ sr}^{-1} \text{ nm}^{-1}). \quad (3.1)$$

2. Irradiance

In contrast to radiance, when measuring or working with units of irradiance, the angular dependence on the amount of radiant energy is removed, and the equation is reduced to radiant energy per unit time, per unit area, per unit wavelength as in Equation [3.2],

$$E(\vec{x}; t; \lambda) \equiv \frac{\Delta Q}{\Delta t \Delta A \Delta \lambda} \text{ (W m}^{-2} \text{ nm}^{-1}\text{)}. \quad (3.2)$$

However, the detectors of interest only receive photons from within a particular hemisphere, thus leading to a hemispherical dependence on irradiance measurements. While this is a sensor limitation, by rotating the sensor 180°, radiation measurements can be made from both hemispheres. For most environmental applications, sensors that measure irradiance are positioned straight up to obtain readings of the sky energy - the downwelling irradiance, and then straight down to obtain a measure of energy emitted and reflected from the Earth's surface - the upwelling irradiance.

3. Reflectance

Two quantities that will be of use are the spectral irradiance reflectance $R(z; \lambda)$ and the spectral remote-sensing reflectance $R_{rs}(\theta, \phi; \lambda)$, defined as Equations [3.3] and [3.4] respectively.

$$R(z; \lambda) \equiv \frac{E_u(z; \lambda)}{E_d(z; \lambda)}, \quad (3.3)$$

$$R_{rs}(\theta, \phi; \lambda) \equiv \frac{L_w}{E_d(z = a; \lambda)} \text{ (sr}^{-1}\text{)}. \quad (3.4)$$

Where E_u and E_d in Equation [3.3] are the spectral upwelling and downwelling plane irradiance, and $R(z; \lambda)$ is evaluated just below the surface of the water. In Equation [3.4]

L_w is referred to as the water leaving radiance and E_d is now evaluated above the surface of the water, so that R_{rs} is a measure of the amount of downwelling light that has returned through the water surface for detection.

4. Radiance Invariance

The radiance invariance law is an important consequence of the measurement. Simply stated, '*Radiance is distinguished by the property that it does not change along a photon path in a vacuum.*', Mobley (1994). This can be illustrated by a geometric example, Figure 3.1, showing two different viewpoints of the same system.

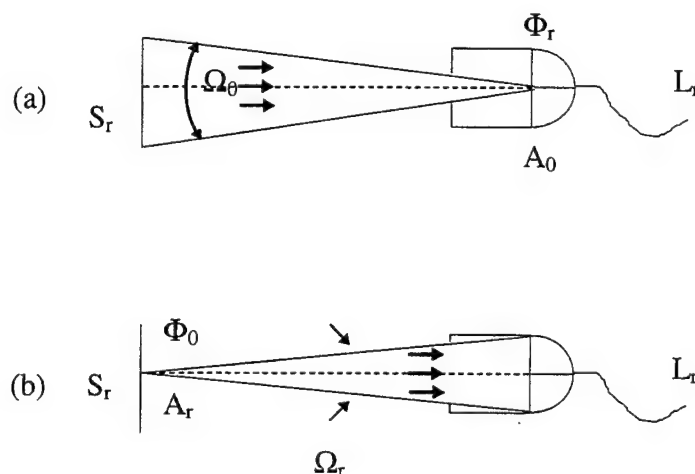


Figure 3.1. Radiance Invariance

In (a) the radiance quotient can be described as $\Phi_r / A_0 \Omega_0$, where Φ_r is the radiant power from the surface S_r , incident on the collection surface, A_0 . The solid angle subtended by S_r at A_0 is Ω_0 and distance between the emitting surface and the collector is r . Conversely in (b), the radiance is described by $\Phi_0 / A_r \Omega_r$, where now the radiant power Φ_0 originates from a point at the surface S_r of variable area A_r , and travels within a bundle confined by the solid angle Ω_r to the collector's surface. In either viewpoint the radiant power

incident on the collectors surface remains unchanged, $\Phi_0 = \Phi_r$. From the definition of solid angle, $\Omega = A / r^2$, Equation [3.5] follows.

$$\frac{A_0 A_r}{r^2} = \Omega_r A_r = \Omega_0 A_0. \quad (3.5)$$

It then follows from the definition of radiance, that

$$L_r = \Phi_r / A_0 \Omega_0 = \Phi_0 / A_r \Omega_r = L_0, \quad (3.6.a)$$

thus

$$L_0 = L_r. \quad (3.6.b)$$

In other words, the distance between the source of emission and the collector does not change the amount of radiation that arrives at the detector. The relations shown in Equation [3.6.a] and [3.6.b] holds as long as the radiation travels within a vacuum. If not a vacuum, the medium through which the radiation travels determines how much of the emitted signal will be attenuated in the journey to the sensor. With this in mind, models can be developed to separate real signals from noise inherent to a particular medium.

B. LIGHT AND HOW IT INTERACTS WITH WATER

As light travels through a medium, it will interact in such a way as to change the characteristics of that light field. Whether these transformations are minor, or extremely significant, is dependent on the nature of the medium. In particular the two mediums that this paper will be interested in are air and water. The atmosphere, although very dynamic and constantly changing, is fairly well understood, and several models have been developed in the past decades that predict light propagation within it. A brief discussion of this interaction and the associated model 'MODTRAN3.5' is presented in section III.C. However, for a more detailed discussion of the subject, the reader is referred to Robinson

(1985), or Stewart (1985). However, water is a denser medium which contains more suspended material in much greater concentration than air. In addition, these concentrations change rapidly over very small spatial dimensions making water a very difficult medium to model. To understand this interaction, one must first understand how the properties of a body of water relate to a light field. Following the reasoning of Mobley (1994), the different properties of water can be divided into essentially two categories; the first being those properties that depend upon the medium itself, defined as *inherent optical properties* (IOP's). The second category is composed of those properties that depend upon both the medium itself and the directional structure of the light field. This second category is defined as *apparent optical properties* (AOP's).

1. Inherent Optical Properties

IOP's can be better understood by first visualizing how light interacts with a small volume of water ΔV and thickness Δr , Figure 3.2.

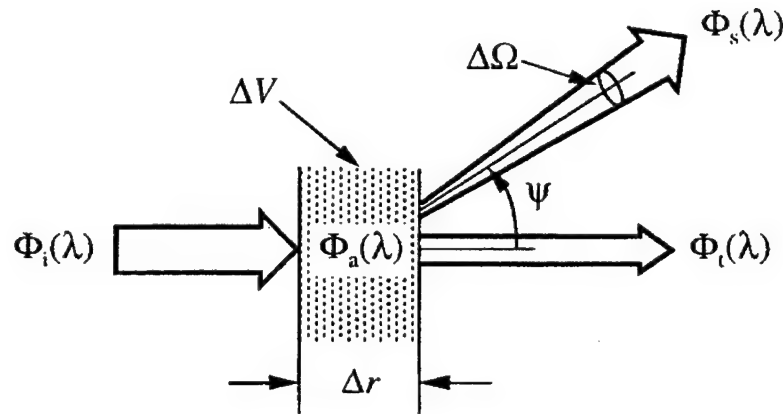


Figure 3.2. Geometry used to define inherent optical properties. From Mobley (1994).

Using the notation of Mobley (1994), $\Phi_i(\lambda)$ is the incident radiant power of a narrow collimated beam of monochromatic light, $\Phi_a(\lambda)$ is the radiant power absorbed by a column of water, $\Phi_t(\lambda)$ is a measure of the radiant power that is transmitted through the

same column of water, $\Phi_s(\lambda)$ is the radiant power that is scattered by the column of water and ψ is the scattering angle. Summing the different terms in accordance with the conservation of energy gives Equation [3.7],

$$\Phi_i(\lambda) = \Phi_a(\lambda) + \Phi_s(\lambda) + \Phi_t(\lambda). \quad (3.7)$$

From this relation such properties as the spectral absorptance coefficient, $a(\lambda)$, the spectral scattering coefficient, $b(\lambda)$, and the spectral beam attenuation coefficient, $c(\lambda)$, can be defined.

a. Spectral Absorptance

The spectral absorptance is defined as the fraction of incident power absorbed within ΔV , Equation [3.8].

$$A(\lambda) \equiv \frac{\Phi_a(\lambda)}{\Phi_i(\lambda)}. \quad (3.8)$$

Then by taking the limit of $A(\lambda)$ divided by the length of the water column Δr Equation [3.9],

$$a(\lambda) \equiv \lim_{\Delta r \rightarrow 0} \frac{A(\lambda)}{\Delta r}, \quad (3.9)$$

with the spectral absorption coefficient $a(\lambda)$ having units of m^{-1} .

b. Spectral Scatterance

The spectral scatterance is similarly defined as the fraction of the incident power that is scattered out of the beam as it passes through the column of water of length Δr , Equation [3.10],

$$B(\lambda) \equiv \frac{\Phi_s(\lambda)}{\Phi_i(\lambda)}, \quad (3.10)$$

and the spectral scattering coefficient $b(\lambda)$ is defined as Equation [3.11],

$$b(\lambda) \equiv \lim_{\Delta r \rightarrow 0} \frac{B(\lambda)}{\Delta r}. \quad (3.11)$$

c. Spectral Transmittance

The spectral transmittance, $T(\lambda)$, is given as the ratio of transmitted power to incident power as in Equation [3.12],

$$T(\lambda) \equiv \frac{\Phi_t(\lambda)}{\Phi_i(\lambda)}. \quad (3.12)$$

$T(\lambda)$ is a measure of the amount of radiative power that passes through a water column.

d. Other Significant Quantities

Several other IOP's are derived from these 3 quantities. The first is simply defined as the sum of the spectral absorption and scattering coefficients and is called the spectral beam attenuation coefficient Equation [3.13],

$$c(\lambda) = a(\lambda) + b(\lambda). \quad (3.13)$$

The beam attenuation coefficient, in turn leads to another important quantity called the optical depth, defined as a measure of the attenuation of energy due to both absorption and scattering, and given by Equation [3.14],

$$\zeta = \int_0^z c(z') dz'. \quad (3.14)$$

Where the beam attenuation coefficient $c(z)$ has been expressed as a function of geometric depth z .

One final quantity of note is called the spectral absorbance – (note not the absorptance). This term is more commonly referred to as the optical density and is given by Equation [3.15],

$$D(\lambda) \equiv \log_{10} \frac{\Phi_i(\lambda)}{\Phi_s(\lambda) + \Phi_t(\lambda)} = -\log_{10}[1 - A(\lambda)]. \quad (3.15)$$

2. Water Constituents

Knowing the IOP's is a very important step in being able to model how a light field will interact with a body of water. However, these properties depend not only on the water itself, but also on the various constituents within the water. It is therefore important to be concerned with the various constituents that make up both fresh and sea water. The main obvious difference between the two is the fact that sea water contains various amounts of dissolved salt. Although these salts do not have significant effect on absorption in the wavebands of interest, namely the visible portion, they do increase the scattering above that of fresh water by approximately 30%. Table 3.1, derived from information in Mobley (1994), lists several of the constituents that may be found in both types of waters, and gives a brief explanation of each. Particulate matter can, in general, be divided into two separate categories based on origin: biological and inorganic sources. Those particles that are of biologic origin include bacteria, phytoplankton, zooplankton and organic detritus (particulate matter left after the death of an organism and organic waste). Inorganic particles enter the water as a result of the erosion of terrestrial rocks or soil.

Table 3.1. Types of water constituents.

Matter Type	Type of Particle	Comments
Organic	Colloids	Contribute significantly to back scattering
	Bacteria	Contributes significantly to particulate backscatter,
	Phytoplankton	Primarily responsible for determining optical properties of most ocean waters.
	Organic Detritus	Primary backscattering component in the ocean
	Zooplankton	Very small living animals
Inorganic	Quartz Sand	Typically very finely ground
	Clay Minerals	

3. Summing the Different Inherent Optical Properties

As described in the last section, water contains many different types of particulate matter. Since each of these will interact with a field of light in a different manner, the inherent optical properties will change as a function of the distribution of particles within a body of water. The water, being a very dynamic entity, also causes the distribution of particles to be very dynamic, and therefore difficult to exactly predict. In particular, it's the sum of the effects that is of interest. By knowing the general absorption and scattering for different particulate matter, the effects can be summed to develop a feel for how the entire body of water will interact with the light field. AOP's can be generally described as a derivative of IOP's that are dependent on both the nature of the medium and the directional structure of the ambient light field.

4. Absorption in Water

When discussing the absorption of light in water, most all of the above mentioned particulate matter play a role, and need to be modeled. The total absorption coefficient

will be the sum of all the different particulate matter coefficients, as well as the inherent absorption due to the electromagnetic (EM) properties of pure water. The models presented below are taken from Mobley (1994).

a. Absorption in Pure Water

For a more complete understanding of EM properties as they relate to substances with different index of refraction, the reader is referred to Klein et al (1986). For the purpose of this text it is assumed that the reader has sufficient background in optics to understand the basic principles of plane wave propagation. To begin, a relationship between the absorption coefficient $a(\lambda)$ and the complex index of refraction $k(\lambda)$ (Also called the Electrodynamic absorption coefficient) is defined by Equation [3.16],

$$a(\lambda) = \frac{4\pi k(\lambda)}{\lambda} \quad (3.16)$$

Where λ is the *in vacuo* wavelength. Figure 3.3, is a representation of how $k(\lambda)$ varies with wavelength.

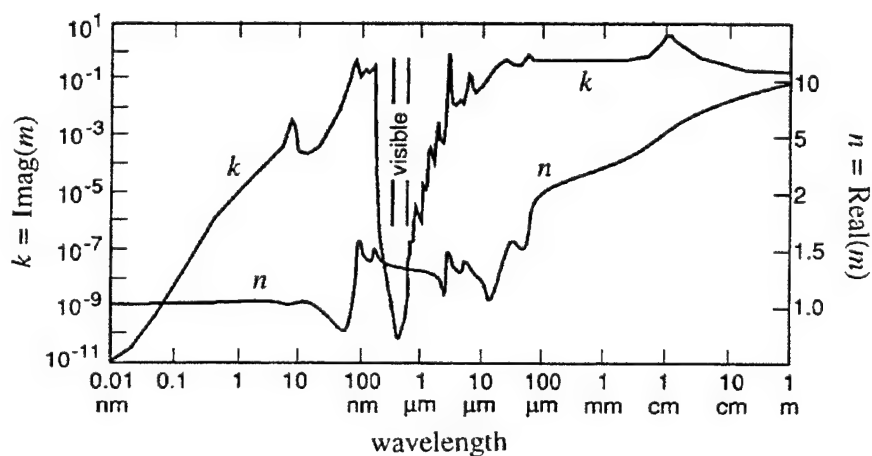


Figure 3.3. Complex (left) and Real Index (right) of refraction in Pure Water verses wavelength. From Mobley (1994).

In addition, Mobley (1994) defines $n(\lambda)$ to be the real part of the complex index of refraction m (where $m = n - ik$). The feature of interest is the nine order of magnitude decrease in $k(\lambda)$ as it passes through the near ultraviolet into the visible, and then rises sharply again as it approaches the near infrared. This characteristic is directly related to the spectral absorption in pure water through Equation [3.16], and is displayed graphically in Figure 3.4.

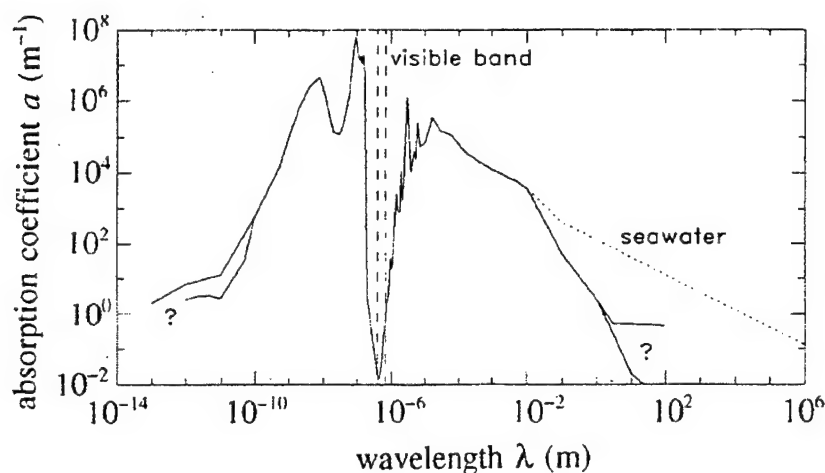


Figure 3.4. Absorption coefficient of pure water (solid line) and pure sea water (dotted line) plotted versus wavelength. From Mobley (1994).

It is this characteristic of pure water and pure sea water that makes shallow water bathymetry possible. However it is also this characteristic that restricts bathymetric measurements to the visible portion of the spectrum. In fact, Figure 3.5 shows that shallow water bathymetry is further restricted to the blue - green portion of the visible spectrum.

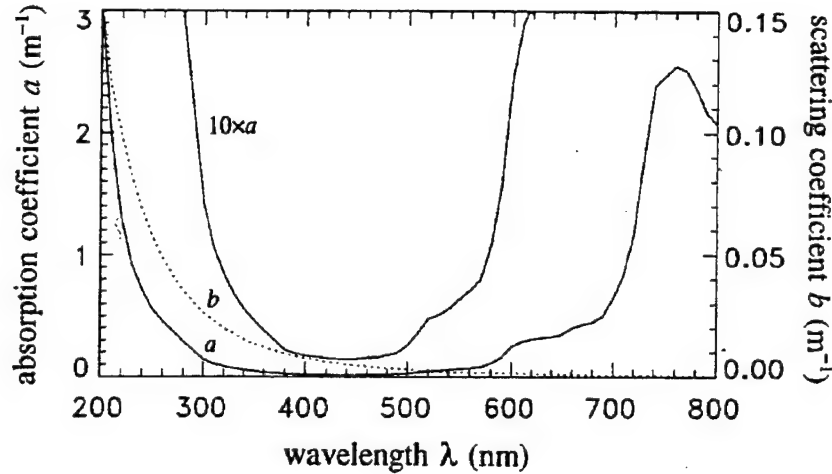


Figure 3.5. Absorption coefficient $a(\lambda)$ (solid line) and scattering coefficient $b(\lambda)$ (dotted line) of pure water plotted versus wavelength. From Mobley (1994).

Figure 3.5 clearly shows a sharp increase in absorption outside the blue - green portion of the spectrum.

b. Absorption Due to Dissolved Organic Matter

Dissolved organic matter, which is commonly referred to as yellow matter, CDOM or gelbstoff, is well understood. Absorption by yellow matter can be modeled fairly closely by Equation [3.17]:

$$a_y(\lambda) = a_y(\lambda_0) e^{-0.014(\lambda - \lambda_0)}. \quad (3.17)$$

Thus, by knowing the initial absorption $a_y(\lambda_0)$ at some characteristic wavelength, usually taken to be $\lambda_0 = 440$ nm, the absorption at all other wavelengths can be modeled.

c. Absorption Due to Phytoplankton and Organic Detritus

Photosynthetic pigments of various types are the major contributors to absorption by phytoplankton, of which chlorophyll is known to be the strongest contributor. Chlorophyll is common to all photosynthetic plants, and therefore as would be expected is a strong absorber of visible light. This effect is particularly strong within the green portion of the visible spectrum. Results from the analysis of several different types of phytoplankton are plotted in Figure 3.6.

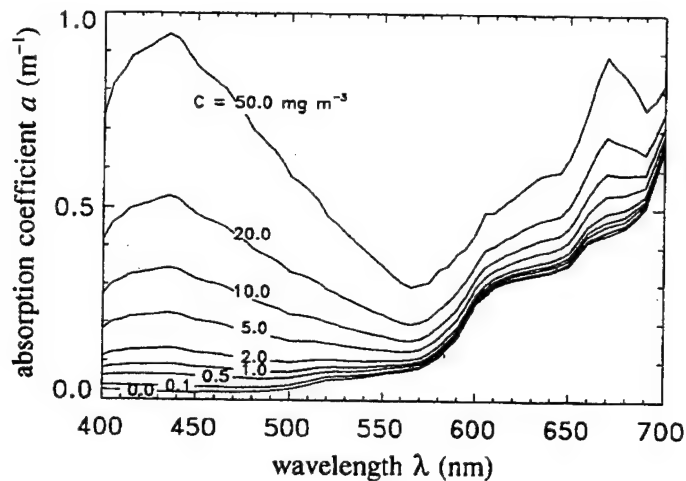


Figure 3.6. Total absorption coefficient for selected chlorophyll concentrations C . From Mobley (1994).

It should be noted that each plot of the absorption coefficient takes on a maximum in the blue portion of the spectrum at 440 nm and in the red at 675 nm, while it takes on a minimum around 600 nm in the green portion of the spectrum. This effect will have significant consequences when trying to derive bathymetric information in areas with a high chlorophyll concentration.

d. Contributions From Sediment

Absorption due to inorganic material, although possibly just as significant as that of organically derived particles, is not well understood. Much of the research in the field of bio-optics has been directed toward understanding the growth of biological constituents in different areas of the ocean. As a result, algorithms have been derived that help to model the optical interaction of light in waters with varying concentrations of organic material. However, comparatively speaking little effort has been put forth in trying to better understand the role of sediment in water. However, for the purpose of clear fresh water, the effects of sediment load will be assumed to be minimal.

e. Deriving a Model for Total Absorption

Several models have been developed that lead to a description of the total spectral absorption coefficient for a given water type, each of which in some way or

another will depend on the definitions above. One algorithm, in particular, will be mentioned at this point, due to the consequences it will have on running the radiative transfer model Hydrolight3.0, to be discussed later. The algorithm presented in Equation [3.18] attempts to model the total absorption $a(\lambda)$, due to all the above terms, and express it in one complete formula.

$$a(\lambda) = (a_w(\lambda) + 0.06a_c^*(\lambda) C^{0.65}) (1 + 0.2 e^{-0.014(\lambda-440)}) \quad (3.18)$$

5. Scattering in Water

Scattering can be defined as the redirection of energy, where as absorption is the removal of energy. EM radiation can be scattered by virtually any of the above mentioned constituents of water. The manner in which it is scattered is a function of a number of different parameters, including particle shape and size, particle index of refraction, wavelength of radiation and viewing geometry. Mie theory characterizes the different types of scattering by what is called the scattering size parameter χ , Equation [3.19]. The Mie parameter is simply a ratio of the circumference of a particle to the wavelength λ of the incident radiation,

$$\chi = \frac{2\pi r}{\lambda}, \quad (3.19)$$

where r is the radius of the particle. As would be expected, for different values of χ the manner in which radiation is scattered will be different. Table 3.2 outlines the different ways in which radiation will be scattered as a function χ .

Table 3.2 Types of scattering based on the scattering size parameter χ .

χ	Type of Scattering
$\chi < 10^{-3}$	Very little scattering
$10^{-3} < \chi < .1$	Rayleigh Scattering
$.1 < \chi < 50$	Mie Scattering
$50 < \chi$	Geometric Scattering

As with modeling absorption, it is very difficult to sort out the different individual effects within different water types. Therefore, several analytical formulas have been developed to model the curves which result from measured data. Several of these models have been detailed in Mobley (1994), and will not be discussed in detail here.

C. RADIATIVE TRANSFER

Prior to understanding a measured signal, you must come to an understanding of the history of the signal, i.e. where it came from and what path it took to arrive at the sensor. The theory of radiative transfer explains the rules that govern the transfer of radiation from one place to another, whether that transfer is through the atmosphere, water or orange paint. The processes that apply to atmospheric modeling are summed together in what is called the atmospheric *Radiative Transfer Equation*, and for our purposes can be expressed in elementary form. Using similar notation to that of Robinson (1985), the radiative transfer equation is expressed as Equation [3.20],

$$L_{\text{Sensor}} = L_{\text{path}} + T L_{\text{sky}} + T L_{\text{water}}. \quad (3.20)$$

Where L_{Sensor} is a measure of the total radiation arriving at the sensor, L_{path} is the atmospheric path radiance, L_{sky} is a measure of the radiance reflected off of the surface, T is the atmospheric transmittance and L_{water} is defined as the water-leaving radiance.

Figure 3.7 depicts the general terms involved and gives a rough idea of the different paths the photons take to arrive at the sensor.

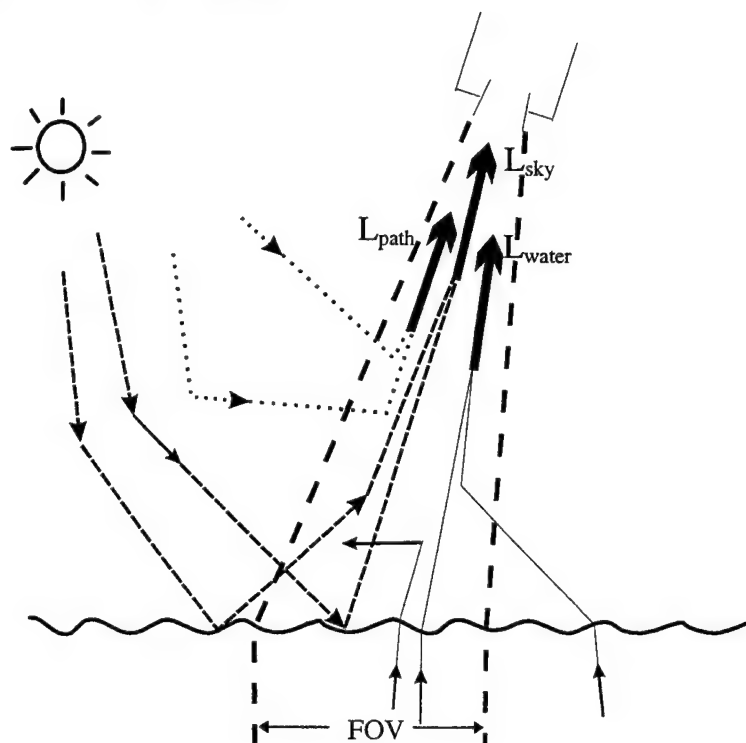


Figure 3.7. Radiative Transfer through the air and water.

The path radiance term is a resultant of all the photons that originated outside of the sensor field of view (FOV) and have been, for one reason or another, scattered by the atmosphere into the FOV. The path radiance terms include the dotted lines that lead to the arrow labeled L_{path} . Radiance that is incident on the water within the sensors FOV and is subsequently reflected or scattered back toward the sensor, can be considered to come from two general terms -- *sun glitter* and *sky glitter*. Sun glitter can be described as that radiation from the sun that is reflected at the sea surface, directly into the FOV. However, sky glitter is scattered by the atmosphere, prior to being reflected off the surface into the FOV. The contributions that make up L_{sky} are represented by the dashed lines in Figure 3.7. The final contribution to the overall radiance measured by the sensor is defined as the water leaving radiance, L_w , which is shown as the solid lines in Figure

3.7. L_w is the sum of those photons that actually enter, interact with and then emerge again, from the water, within the sensors FOV.

As briefly mentioned earlier, MODTRAN3.5 is a radiative transfer model that will model the atmospheric effects discussed above. MODTRAN3.5 is the latest generation of atmospheric modeling programs developed by Phillips Laboratory. BETA restrictions were lifted as of December 1996. At the time this thesis was written, a substantial reference for MODTRAN3.5 was not available. However Phillips Laboratory cited Berk et al. (1996), which is a paper that had been submitted for publication. A complete discussion of the parameters used for the modeling of Lake Tahoe will be provided in Chapter IV.

1. Radiative Transfer at the Water

Once atmospheric effects are understood and modeled, L_w can be derived. The next step is to model the radiative transfer process within the water itself. However, this is very difficult as the radiation is effected by scattering at the surface of the water, absorption and scattering within the water column and scattering and attenuation of the bottom material. All of which are extremely complex and constantly varying.

Mobley (1994) presents a complete and thorough discussion of the process of radiative transfer within the water. HYDROLIGHT 3.0, which was developed by Dr. Curtis D. Mobley, can be used to model a variety of different aquatic environments based on many of the parameters explained above. The more information a user is able input into the code concerning the particular makeup of a body of water, the more accurate the results will be. A discussion of the inputs used for Lake Tahoe will be given in Chapter V. As will be pointed out later, the parameter of interest, within the water, will be the wavelength dependent diffuse attenuation coefficient (K_d). Figure 3.8 is Figure 8 from Mobley (1995) and is provided as an example of HYDROLIGHT's ability to compute K_d .

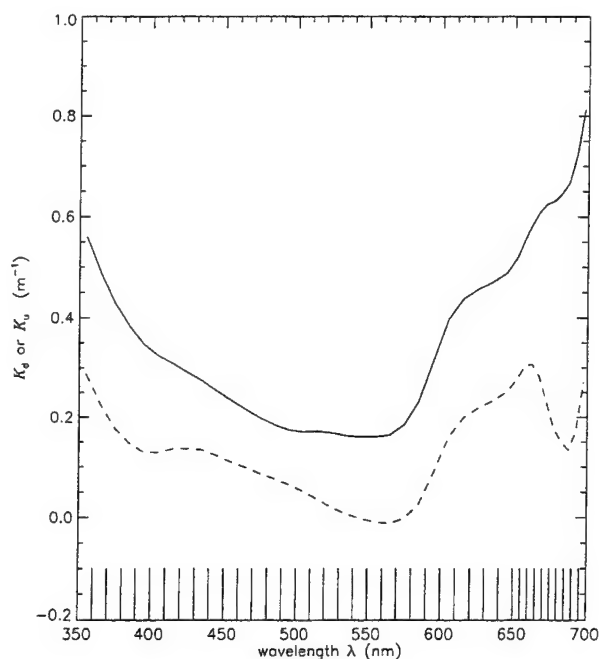


Figure 3.8. Example of modeled K_d .
Figure 8, from Mobley (1995).

The values for $K_d(\lambda)$ upwelling (dotted line) and $K_d(\lambda)$ downwelling (solid), plotted in Figure 3.8, are calculated for pure water which also contains such particulate matter as colored dissolved organic matter and chlorophyll-bearing particles.

D. BATHYMETRY FROM REMOTELY SENSED RADIATION

1. Unmixing Effects Due to Depth and Substrate Reflectance - The Bierwirth Algorithm - An Exploitation of LANDSAT Data

Water leaving radiance is the amount of radiation upwelling from within the water column. This upwelling radiation is the sum of radiation incident off of the substrate and the radiation which is due to the bulk reflectance of the water. Let L_w be the water leaving radiance, L_s the radiance of the wet substrate material, as if there were no water cover, L_{dw} the radiance due to the bulk reflectance of the water column (i.e. deep water radiance) and, as before, T_w the transmittance within the medium. Following the method

of Jupp (1988), and Bierwirth et al. (1993), the preceding terms can be combined to form Equation [3.21],

$$L_w = T_w L_s + (1 - T_w) L_{dw} . \quad (3.21)$$

This expression now takes into account all of the scattering and absorption of the water column by combining them into the one term T_w . If T_w is normalized so that it varies between 0 and 1, it then becomes a fraction for the amount of radiation the body of water allows to pass. T_w then takes the form of

$$T_w = e^{-2K_d z} . \quad (3.22)$$

K_d is the attenuation coefficient and z is the depth. Equations [3.21] and [3.22] are not exact, but come very close to modeling the way in which radiative transfer takes place. Jupp, therefore, argues that they sufficiently model the radiative process within the water studied. Equation [3.23] is the result of combining Equations [3.21] and [3.22],

$$L_w = L_{dw} + (L_s - L_{dw})e^{-2K_d z} . \quad (3.23)$$

Bierwirth (1993), follows a similar development to that of Jupp (1988) up to this point. Bierwirth then seeks to unmix the effects due to reflectance with those due to depth, by deriving a substrate reflectance factor for each band processed. He begins, by normalizing Equation [3.23] to reflectance values, as in Equation [3.24]

$$R_w = R_{dw} + (R_s - R_{dw})e^{-2K_d z} . \quad (3.24)$$

Assuming that the deep-water reflectance is small compared to the substrate reflectance, Equation [3.24] can be expressed as Equation [3.25],

$$R_{wi} - R_{dwi} = R_{wi}' = R_{si}e^{-2K_{di}z} ; \quad i = 1, N. \quad (3.25)$$

Where R_w' is the water leaving reflectance, corrected for deep water, the i-subscripts specify a wavelength dependence and N is the number of wavelength measured. Notice, that for ideal measurements over deep water, $R_{wi} = R_{dwi}$ and Equation [3.25] will be zero. This indicates that all of the reflectance from the substrate is attenuated.

Solving for depth z in Equation [3.25], gives Equation [3.26],

$$z = \frac{\ln(R_{wi}')}{-2K_{di}} - \frac{\ln(R_{si})}{-2K_{di}}; i = 1, N. \quad (3.26)$$

For Equation [3.26], the N values of R_{si} are unknown as is the depth, giving a total of N+1 unknowns that need to be sorted out. A unique solution is unlikely. However, by taking a linear combination of all the wavelength dependent equations and assuming the geometric mean of the substrate reflectance equals one, a solution for the estimated depth falls out. This assumption is equivalent to letting the second term on the right hand side of Equation [3.26] equal zero. The resultant is Equation [3.27];

$$Z = \sum_{i=1}^N \frac{\ln(R_{wi}')}{-2K_{di}N}. \quad (3.27)$$

Bierwirth et al. (1993), in applying Equation [3.27] to multispectral LANDSAT data taken over Hamelin Pool, Shark Bay, Western Australia has been able to produce an estimated depth image, Figure 3.9.a, and 3.9.b. Artificial illumination has been applied in Figure 3.9.b to get a better idea of the detailed structure that has been derived. For comparison, Figure 3.9.c depicts a true depth image of the pool resulting from hydrographic survey. Z, the estimated depth, has an error of Δz . A primary contribution to this depth error is the assumption of an overall bright bottom, which results in the inaccurate report of depth over areas of dark substrate

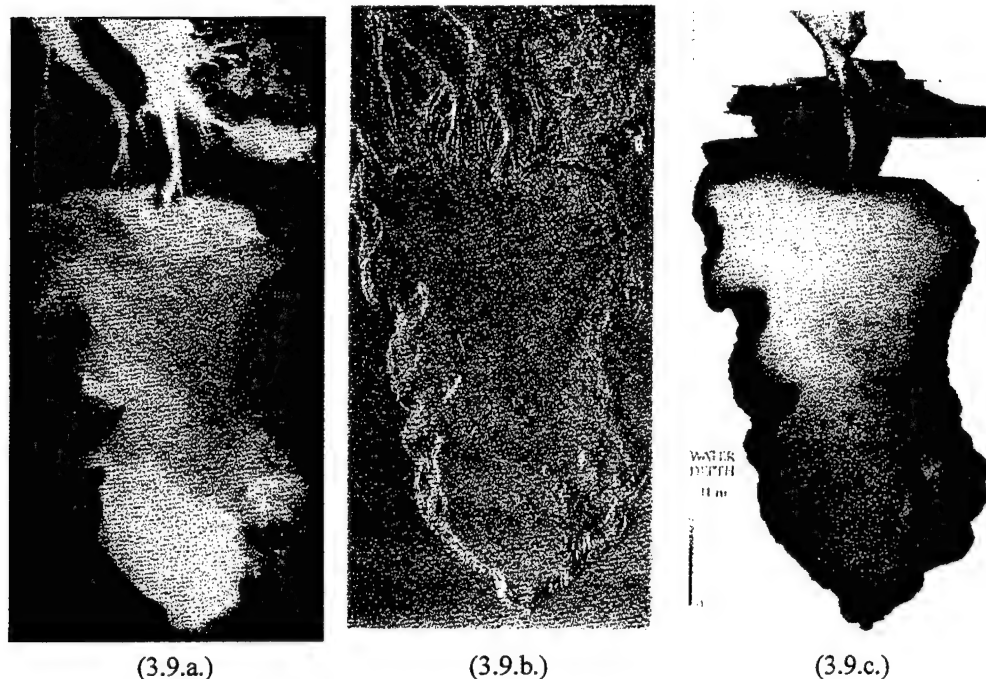


Figure 3.9. Derived and measured bathymetry for Hamelin Pool, Bierwirth et al. (1993).

In comparing Figure 3.9.a and 3.9.c, Bierwirth et al. point out that the two are linearly correlated “reasonably” well. However, he also makes the point that, in regions of dark substrate (i.e. near the bottom and in the in the tidal channels near the top), the depth is exaggerated.

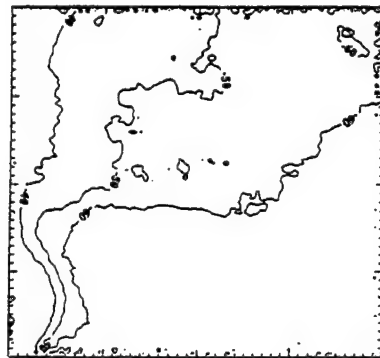
2. Empirical Model - Hamilton Algorithm - An Application of AVIRIS Data

A more empirical approach is possible. Hamilton et al. (1993) estimate depth in Lake Tahoe using an empirical model of the form.

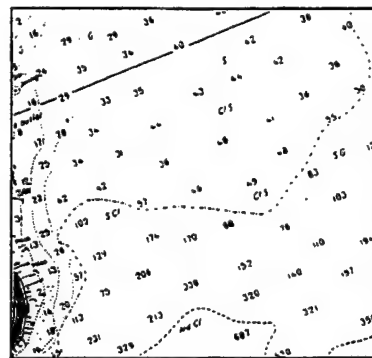
$$Z = a_0 + a_1(R_{rs}(\lambda_1)) + a_2(R_{rs}(\lambda_2)). \quad (3.28)$$

Where R_{rs} is the remotely sensed reflectance at a particular wavelength, as defined by Equation [3.4] and a_0 , a_1 and a_2 are the linear coefficients. To determine these linear

coefficients for Lake Tahoe, Hamilton et al. explain that the surface spectra was taken and compared along a transit line of varying bottom depth. Two wavelengths were then chosen that displayed a large amount of variance in instrument response, $\lambda = 490$ nm and $\lambda = 560$ nm. The application of a multiple regression revealed the linear coefficients to be $a_0 = 34.96$, $a_1 = 23.36$ and $a_2 = 34.64$ with a multiple correlation coefficient of 0.96. Figure 3.10.a is a contour plot of AVIRIS data taken over a portion of Lake Tahoe from Hamilton et al.. For comparison, Figure 3.10.b shows the charted depth of the same region.



(3.10.a)



(3.10.b)

Figure 3.10. A comparison of the depth derived from the Hamilton algorithm (3.10.a) to the charted depth (3.10.b) for a region of Lake Tahoe. Hamilton et al. (1993).

As Hamilton et al. concludes, the two scenes are not exact, but do agree in some of the major features such as the 60 ft. depth curve.

IV. MEASUREMENTS AT LAKE TAHOE

A. MEASUREMENTS AT LAKE TAHOE

Due to the complexity of the water environment, as described in the last chapter, the best place to start deriving bathymetric estimates with data from passive sensors is from a relatively clear environment. Lake Tahoe, which is located on the California-Nevada border high within the Sierra-Nevada mountains provided the ideal conditions to begin developing a model for shallow water bathymetry. As explained in Kappus et al. (1996), the experiment was conducted on June 22, 1995, on a calm, clear day with very little atmospheric aerosols present. Lake Tahoe is 1906 m high at a latitude of 39.14°N, and a longitude of 120.19°W, and can be considered a fairly homogeneous body due to minimal runoff from rivers and low chlorophyll values (less than $.2 \text{ mg m}^{-3}$). The lake, at the time, was extremely clear. The data was taken at approximately 10:05 am to avoid sun glint off of the water, with an aircraft flight path of approximately 100°. This flight path was chosen to correspond with the azimuth angle of the sun at the time, again trying to minimize sun glint off of the waters surface.

B. INSTRUMENTS

Two instruments were flown at Lake Tahoe the day the experiment took place; Hyperspectral Digital Imagery Collection Experiment (HYDICE) and the Airborne Visible infrared Imaging Spectrometer (AVIRIS). For the purpose of this paper, the focus of the discussion will be the use of HYDICE. HYDICE utilizes onboard and laboratory based calibration to convert measured raw digital numbers to physical units of radiance. HYDICE, which is fitted to fly onboard a Convair-580 aircraft, has a swath that varies from 0.2 km to 1.15 km, dependent on the altitude of the aircraft. For the experiment conducted over Lake Tahoe, the aircraft was flown at an altitude of 2.35 km (5,000 ft) above the lake, which resulted in a swath of 0.385 km and a corresponding resolution of

1.2 m. Kappus et al. (1996) points out that this altitude was chosen for a number of reasons, including minimizing atmospheric effects, flight path alignment, choice of swath width and to allow sufficient collection time.

V. INITIAL MODEL APPLICATION

The HYDICE image of Lake Tahoe was obtained from the HYDICE office on a distributed HYDICE 1995 Demonstration Tape, along with several other significant scenes taken that year, Table 5.1. Table 5.1 list the tape information on the HYDICE 1995 Demonstration Tape, with scene of interest in bold type.

Table 5.1. HYDICE 1995 Demonstration Tape Information

File	Mission	Label	Run	Altitude
1	N/A	"support"		
2	950629	"Yuma, AZ"	2	6514'
3	950622	"Lake Tahoe, NV"	4	14,544'
4	950622	"Cuprite, NV"	23	25,982'
5	950829	"Aberdeen, MD"	31	10,111'

The scene was written to an 8mm tape in the form of pre-processed radiance data, with units of $(\text{Watts m}^{-2} \text{ sr}^{-1} \mu\text{m}^{-1})$. Initial analysis and display was completed by utilizing the Interactive Data Language (IDL) produced by Research Systems, Inc., Boulder, CO. In addition, extensive use of The Environment for Visualizing Images (ENVI), which is also a product of Research Systems, Inc., and runs in the IDL environment. The next two sections will consist of an initial analysis of the data utilizing the Bierwirth et al. (1993) algorithm and the Hamilton et al. (1993) algorithm. This initial analysis is done to get a general idea of how the data responds to the different algorithms, thereby giving an indication of how to proceed with the final analysis.

A. APPLICATION OF THE BIERWIRTH METHOD TO LAKE TAHOE DATA

1. Processed HYDICE Data

Figure 5.1, is a 320 by 320 pixel display of radiance data taken at Secret Harbor on the eastern side of Lake Tahoe, and is displayed as a RGB (Red - Green - Blue) image, with the Red wavelength set to 650 nm, the Green wavelength set to 550 nm and the Blue wavelength set to 450 nm. Selecting the wavelengths in this manner, allows the scene to be displayed as a simulated true color image to give the reader a qualitative impression of the scene.

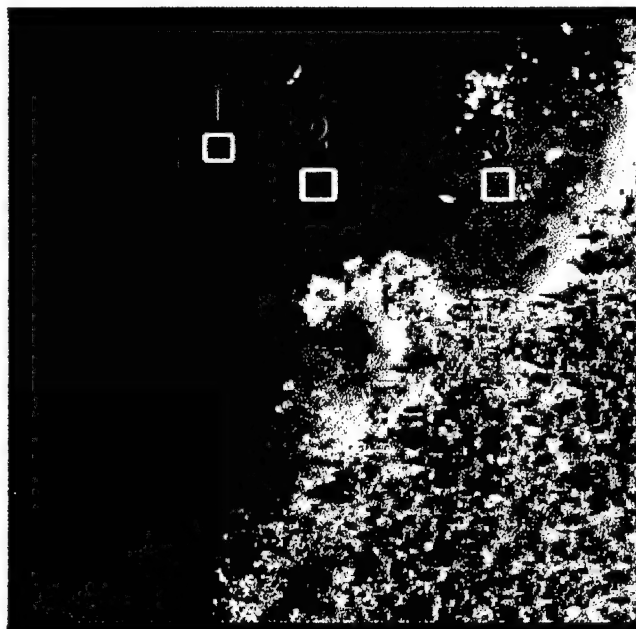


Figure 5.1. Raw data image, displayed with ENVI.

Within the scene, shown in Figure 5.1, are regions that have been highlighted by white rectangles to display areas in which information for initial data analysis were taken. The region labeled 1, was taken over an area of relatively deep water, while regions 2 and 3 were respectively taken over areas of rocky and shallow substrate. These regions provide

enough contrast in relation to each other to sufficiently test ability of the algorithm presented in Bierwirth et al. (1993), to predict depth. Three pixels were chosen, one from each highlighted box in Figure 5.1, for analysis. A line plot of the spectrum for each of the three data points, Figure 5.2, indicates a distinct difference in the amount of radiance data received at the sensor for each of the different pixels, with the lowest radiance values coming from the rocky substrate and the highest values coming from the shallow water over a sandy bottom.

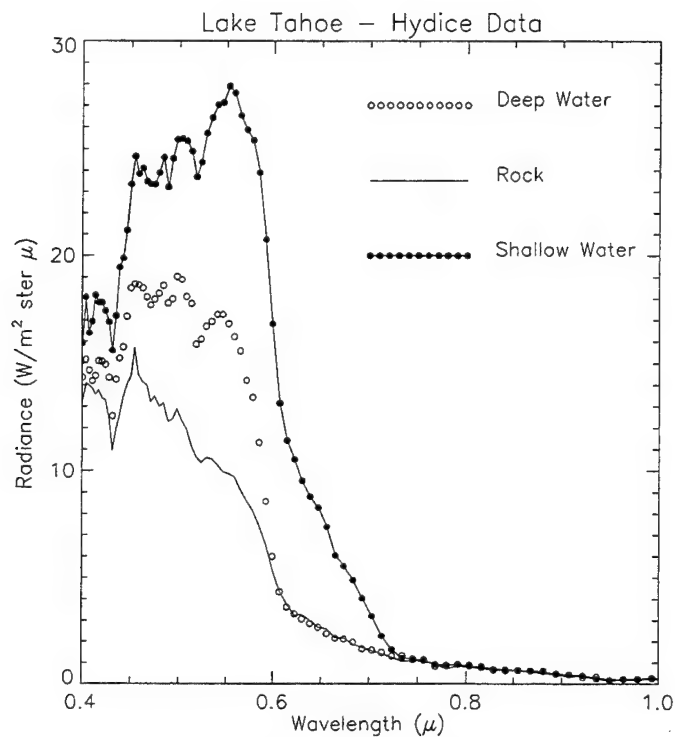


Figure 5.2. HYDICE Spectra for Three Contrasting Pixels.

Notice how the radiance values for each pixel are centered through the blue - green portion of the visible spectrum, as would be expected from previous arguments.

2. Atmospheric Contributions

The first step in deriving bathymetry is to correct the sensor radiance for atmospheric effects. MODTRAN3.5 (Beta version 1.0), radiative transfer code was used to model the atmosphere at the time of the experiment. Listed in Table 5.2 are several of the parameters used for the different runs made with MODTRAN3.5.

Table 5.2. MODTRAN3.5 parameters used to model Lake Tahoe

Run Type	Path Radiance	Sky Radiance
Cards Used	1, 1A, 2, 3, 3A1, 3A2, 4, 5	1, 1A, 2, 3, 3A1, 3A2, 4, 5
Parameters		
Visibility	120 km	120 km
Ground Altitude	1.905 km	1.905 km
Initial Height	4.25 km	N/A
Final Height	1.905 km	N/A
Tangent Height	N/A	1.905 km
Viewing Angle	180°	N/A
Scattering	Mie	Mie
Julian Day	173	173
Latitude	39.14°	39.14°
Longitude	120.19°	120.19°
Greenwich Time	17.08z	17.08z
Frequency Range	10,000 - 25,000 cm ⁻¹	10,000 - 25,000 cm ⁻¹
Frequency Step Size	15 cm ⁻¹	15 cm ⁻¹

a. Path Radiance

Inputting the above parameters, MODTRAN3.5 was first run in radiance mode. Assuming that the sensor was looking straight down at the lake, the path radiance L_{path} was computed. Figure 5.3 is the resultant spectra for the modeled path radiance.

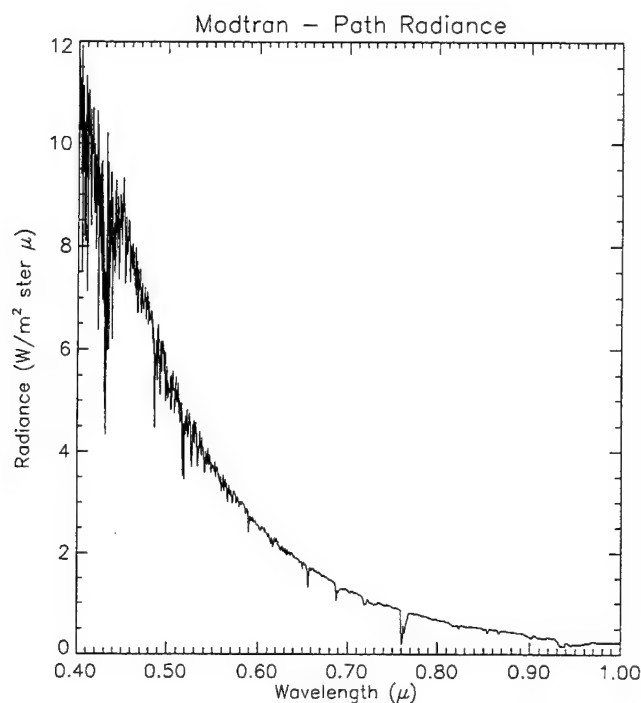


Figure 5.3. Modeled Path Radiance for Lake Tahoe, June 22, 1995.

b. Sky Radiance

Next, the sky Radiance L_{sky} (described in section II.C) was computed, by running Modtran3.5 with the sensor located at the surface, looking up toward the sky. The resultant spectra is plotted as Figure 5.4.

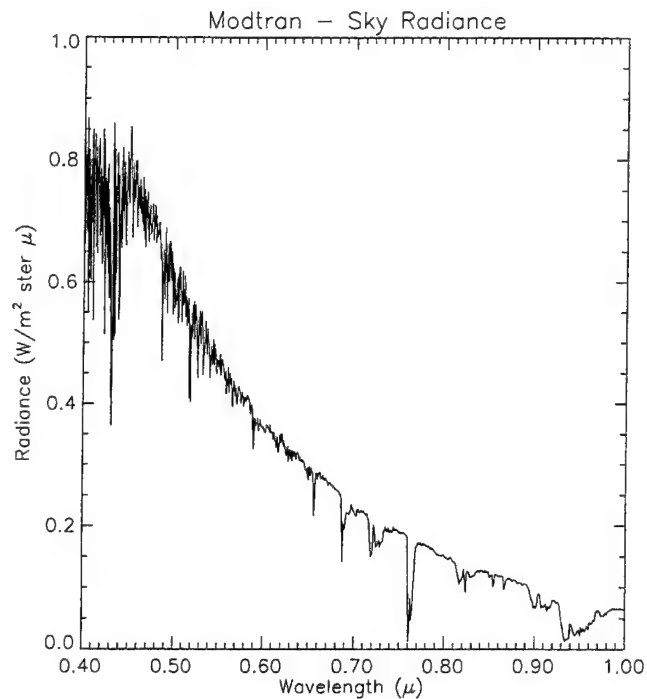


Figure 5.4. Sky Radiance Computed from Modtran3.5, Lake Tahoe, June 22, 1995.

c. Convolving Modtran3.5 Data to Match HYDICE

HYDICE has 79 measurement bandwidths of variable width between .4 and 1.0 μm while Modtran3.5 computes the radiance for around 1000 bandwidths. It is therefore necessary to convolve the modeled spectra to the spectral coverage of the HYDICE sensor. Figure 5.5, is a plot of the sum of path and sky radiance before and after it has been converted to HYDICE wavelengths. The convolved spectrum is plotted as a solid line.

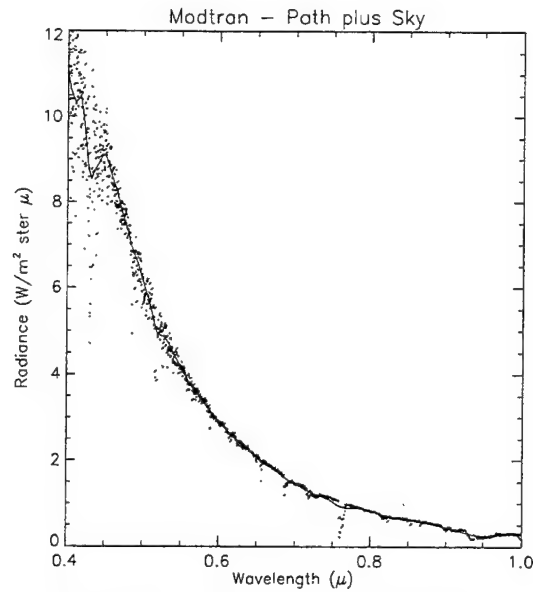


Figure 5.5. Convolved Path and Sky Radiance, Lake Tahoe, June 22, 1995.

To compute the water leaving radiance L_{water} the wavelength dependent atmospheric transmittance T_{atm} is also needed. T_{atm} was computed as part of the path radiance run of Modtran3.5. Figure 5.6, is a plot of the modeled transmittance before and after it was convolved to the wavelengths of HYDICE.

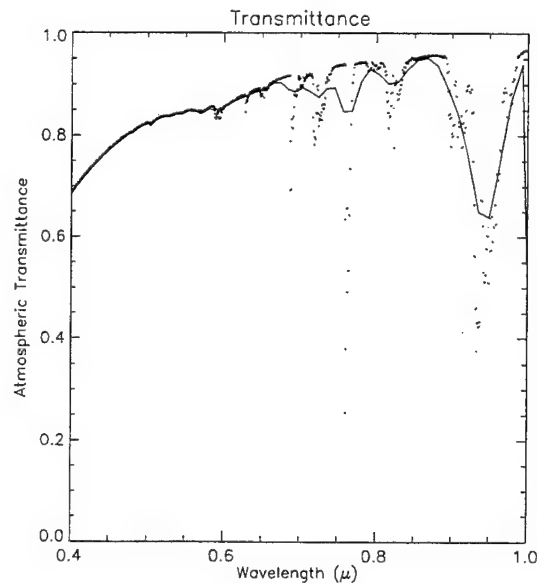


Figure 5.6. Convolved Transmittance, Lake Tahoe, June 22, 1995.

d. Water Leaving Radiance

To compute water leaving radiance for the HYDICE spectrum, it is best to look back at Equation [3.20]. However, now the radiative transfer equation must be expressed as a function of wavelength as in Equation [5.1],

$$L_{\text{sensor}}(\lambda) = L_{\text{path}}(\lambda) + T_{\text{atm}}(\lambda) L_{\text{sky}}(\lambda) + T_{\text{atm}}(\lambda) L_{\text{water}}(\lambda). \quad (5.1)$$

Solving for L_{water} gives Equation [5.2],

$$L_{\text{water}}(\lambda) = \frac{L_{\text{sensor}}(\lambda) - L_{\text{path}}(\lambda) - T_{\text{atm}}(\lambda) L_{\text{sky}}(\lambda)}{T_{\text{atm}}(\lambda)}. \quad (5.2)$$

Substituting the modeled radiance values and the measured radiance of the three selected data points into Equation [5.2], results in the water leaving radiance curves of Figure 5.7.

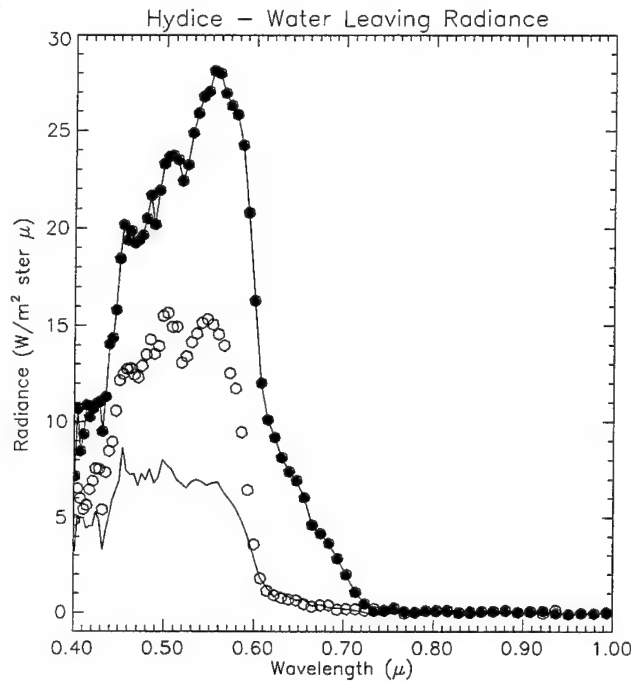


Figure 5.7. Water Leaving Radiance, as computed for three contrasting data point, shallow-water, deep-water and rocky terrain.

As with Figure 5.2, the radiance from shallow water (plotted as dark circles with a solid line) is the highest, followed by the radiance from deep water (plotted as open circles) and the radiance from the rocky region (plotted as a solid line). Recall that at higher wavelengths electromagnetic radiation is almost completely absorbed (i.e. $L_w = 0$). In fact by observing the radiance values in Figure 5.2 it is seen that this effect is true and that corrections for atmospheric effects are reasonably accurate.

e. Normalizing to Reflectance

At this point it is most convenient to work with reflectance instead of radiance. Therefore, following Equation [2.4] a model of the downwelling irradiance $E_d(\lambda)$ must be computed. This was again accomplished utilizing Modtran3.5 run in irradiance mode. After convolving the data to HYDICE wavelengths the irradiance was found as a function of wavelength, Figure 5.8.

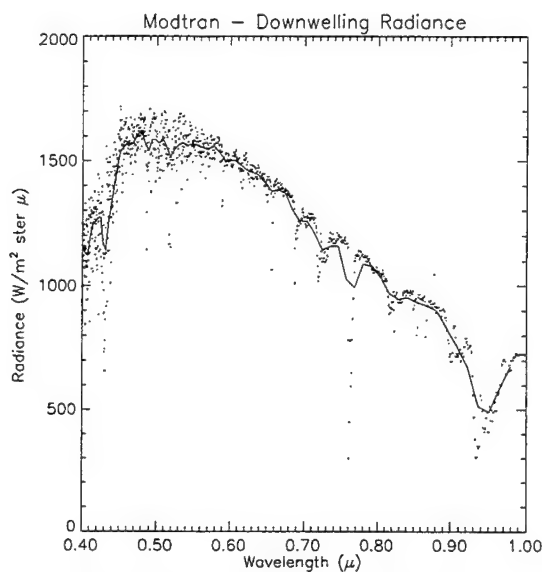


Figure 5.8. Down-welling Irradiance, modeled for Lake Tahoe, June 22,

The remote sensing reflectance, R_{rs} , is found by dividing the water leaving radiance, $L_{water}(\lambda)$, by the down-welling irradiance, $E_d(\lambda)$. Figure 5.9 is a plot of R_{rs} for the three data points of interest.

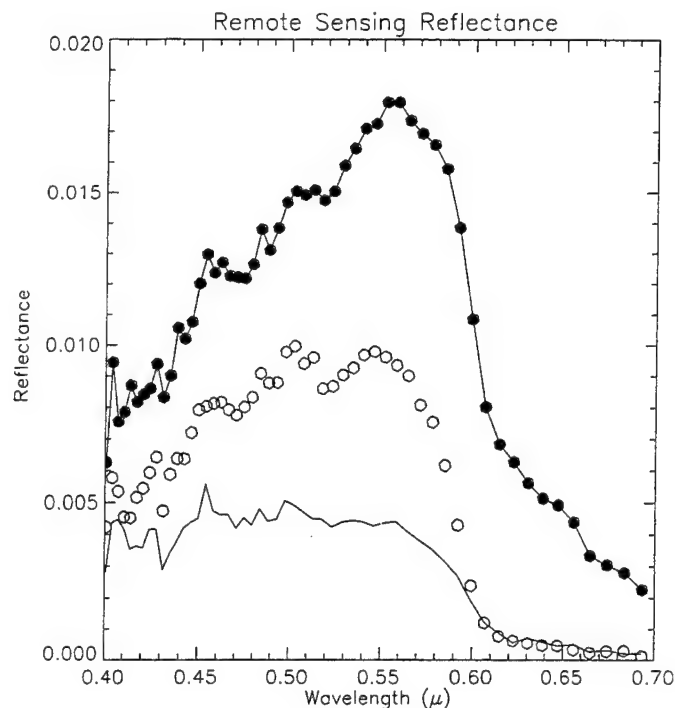


Figure 5.9. Remote Sensing Reflectance, Lake Tahoe, June 22, 1995.

The remote sensing reflectance, R_s , value will in general vary between 0 and 1, and. Here reflectance varies between 0 and .018.

3. Depth Derivation

Several properties of the water must be known in order to use the method of Bierwirth (1993) to derive depth from R_s . In particular, to apply Equation [2.27] the values for the wavelength dependent attenuation coefficients K_d must be known, or at least modeled for the water in question. The radiative transfer model HYDROLIGHT3.0 was used to carry out the model of the K_d values within the water. Table 5.3 presents several parameters that were input into HYDROLIGHT3.0.

Table 5.3. HYDROLIGHT3.5 parameters used to model Lake Tahoe

Parameter	Run Value
Wavelengths	HYDICE Central Wavelengths
Julian Day	173
Latitude	39.14°
Longitude*	-120.19°
Pressure	17.65
Aerosols	5.0
Humidity	10 %
Precipitation	.8 %
Visibility	120.0 km
Average Chlorophyll concentration	0.2 mg m ⁻³
* West Longitude is expressed as negative.	

Several of the above listed parameters are “hard wired”, so to speak, within the file ‘qarealsky.f’ and must be altered to match the particular environmental conditions of interest.

a. HYDROLIGHT, a Radiative Transfer Model

Inputting the above parameters, HYDROLIGHT was used to determine $K_d(\lambda)$. Figure 5.10, is a plot of the modeled attenuation coefficients that have been convolved to the wavelengths of HYDICE.

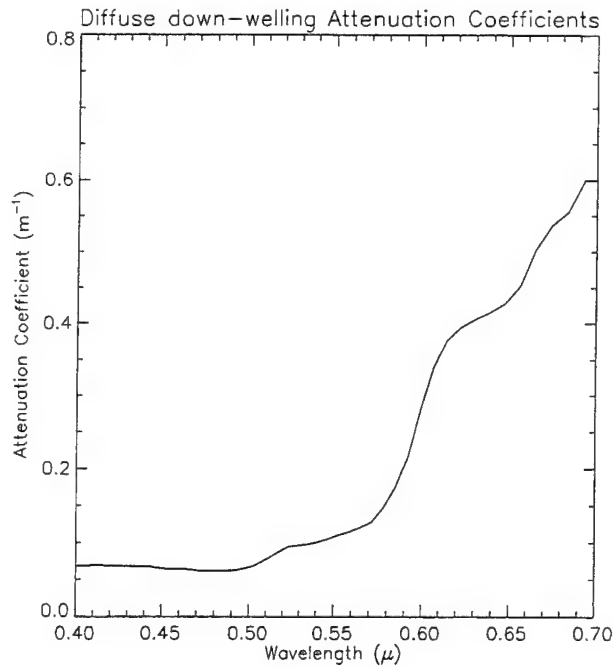


Figure 5.10. Attenuation Coefficients $K_d(\lambda)$, as modeled by HYDROLIGHT.

It should be kept in mind, however, that determination of the attenuation coefficients is currently one of the most difficult parts of the problem, and a wealth of research is still underway to figure out the best way to model these values. For the moment, this paper will assume that HYDROLIGHT has sufficiently modeled K_d , and therefore, use the above values to continue the analysis of the Bierwirth method. The sensitivity of the results for the K_d values will be examined at the end of the next chapter.

b. Results of Bierwirth

Substituting the above modeled values for $K_d(\lambda)$ in Equation [3.27] for K_{di} , where the subscript 'i' indicates the wavelength dependence, the estimated depth can be derived for each of the three data points, Table 5.4.

Table 5.4. Depths, derived from Equation [3.27], for 3 separate data points.

Data Point	Bierwirth Depth
Shallow Water	23.8 m
Deep Water	26.9 m
Rocky Area	29.6 m

The values given in Table 5.4 are indicative of assuming a constant bottom reflectance R_s . The results in the data, as expected contain a large Δz factor for each depth. The relative depth results for areas over sandy substrate are relatively well behaved. However by assuming a uniform bottom type, there is no way to differentiate between deep water and dark rock. As a result, the calculated depth over the rocks is deeper than that of deep water, resulting in unsatisfactory results.

B. APPLICATION OF THE HAMILTON METHOD TO LAKE TAHOE DATA

In applying the method of Hamilton et al. (1993), the remote sensing reflectance R_{rs} , as explained previously, was computed for the entire scene at similar wavelengths to those used in Hamilton et al. Using these computed scene values for R_{rs} , Equation [3.28] and the values for a_0 , a_1 and a_2 given in section III.E.2 a contour plot of the Secret Harbor region of Lake Tahoe can be generated, Figure 5.11.a and compared to published soundings Figure 5.11.b.

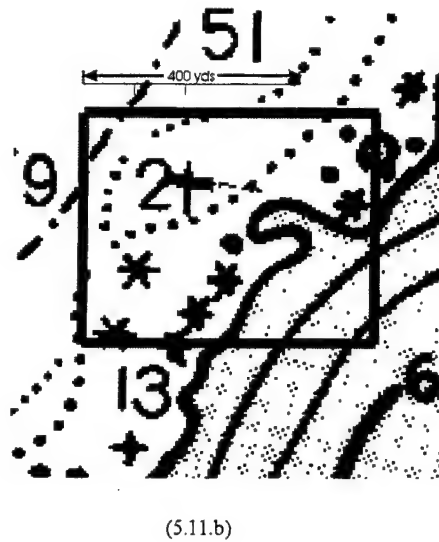
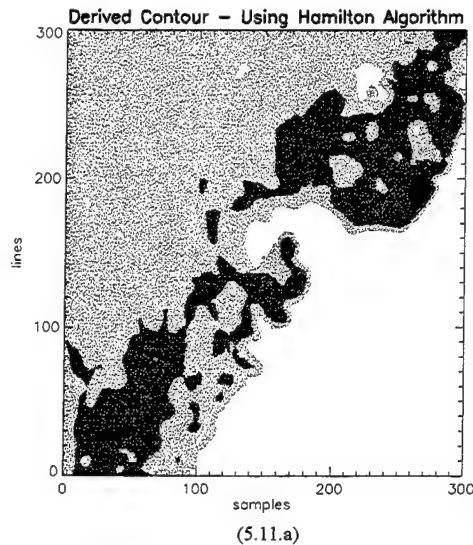


Figure 5.11. Comparison of contour plot derived from Hamilton et al. (1993) algorithm to published soundings of the same region of Lake Tahoe.

The light colors within this scene represent shallow water as the darker colors represent deeper water (white is zero). Therefore, for this scene the Hamilton et al. (1993) algorithm has computed the depth to be the deepest near the shore and the shallowest further off shore (where white is land). Comparing this to published soundings of the same area within Lake Tahoe it is seen that these results are incorrect. To correctly apply this algorithm to the Secret Harbor data, apriori depth information would be needed to derive the applicable correlation coefficients. However, due to the large amount of variation within the substrate of the scene, it would be difficult to establish any solid correlation coefficients that apply to the entire scene. Therefore depth results would still be incorrect.

VI. DERIVING DEPTH WITH MODELED BOTTOM TYPES

As a result of the discussion in the previous sections, it can be surmised that a lack of information about the bottom type will result in a depth error when attempting to apply the Bierwirth et al. (1993) model to a scene. Therefore, to compute accurate depth results, substrate reflectance must be sorted out. This is a difficult task when only a few wavebands of information are available, such as in Landsat or other multispectral instruments. However, by taking advantage of the wealth of information available in a hyperspectral data cube, sorting out the bottom types within a scene becomes much more feasible.

A. MASK CONSTRUCTION

The HYDICE scene of Lake Tahoe contains a large portion of land, as can be viewed in the bottom, right hand, corner of Figure 6.1. The radiant information from land, however, is considered noise for the purpose of analyzing the water column within the scene and therefore should be removed prior to performing any significant analysis.

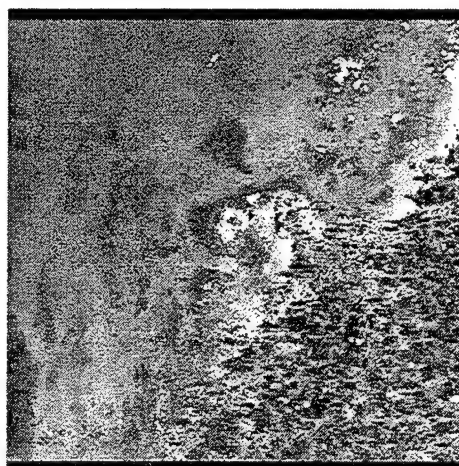


Figure 6.1. Lake Tahoe, 320 x 320 pixel data scene. (Displayed at wavelength 0.5 μ m)

When viewing a scene at wavelengths on the order of $.7\ \mu\text{m}$ and longer, virtually all of the radiation that enters the water is immediately absorbed and never makes it's way back out (i.e. appears black), Figure 6.2. Hence, at these longer wavelengths, the land and the water can easily be differentiated, and a mask of the land created, Figure 6.3 (land pixels have been set to black).



Figure 6.2. Lake Tahoe, 320 x 320 pixel data scene. (Displayed at wavelength $1\ \mu\text{m}$)

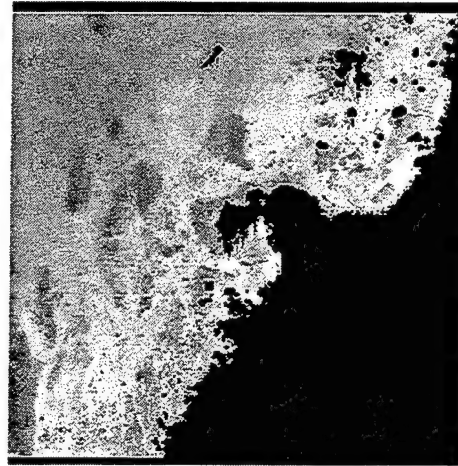


Figure 6.3. Lake Tahoe - Masked data scene. (Displayed at wavelength $550\ \text{nm}$)

A plot of the correlation within each waveband, Figure 6.4, for the masked scene, now shows what one would expect for a scene that contains only water. Figure 6.4 shows that a large amount of information (high correlation coefficient) is contained in the visible wavebands around the blue-green portion of the spectrum ($.4 - .6\ \mu\text{m}$) and very little information (low correlation coefficients) is contained within the red portion of the spectrum and beyond ($> .6\ \mu\text{m}$).

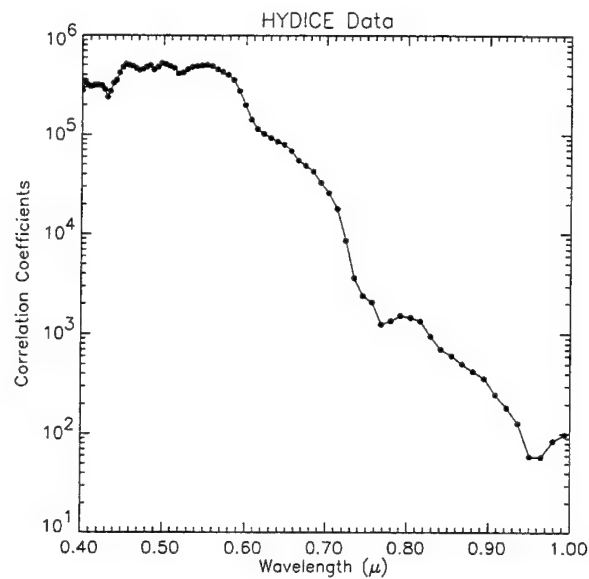


Figure 6.4. Correlation between data points within each wave band.

A principal component analysis (PCA) can now be performed on the masked scene to extract significant information. A plot of the eigenvalues of each of the principle component bands, Figure 6.5, indicates a high degree of variance within the first few bands with very little information in bands 5 and beyond.

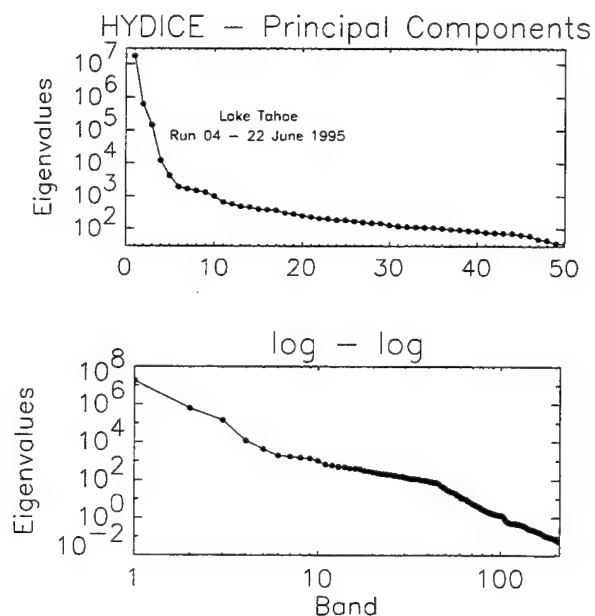


Figure 6.5. Correlation between data points within principal component space.

This four order of magnitude decrease in correlation indicates the relative volume of information contained in each transformed waveband. Figure 6.6 shows the relative weighting of the observed radiance data contributions to three of the first four PC bands.

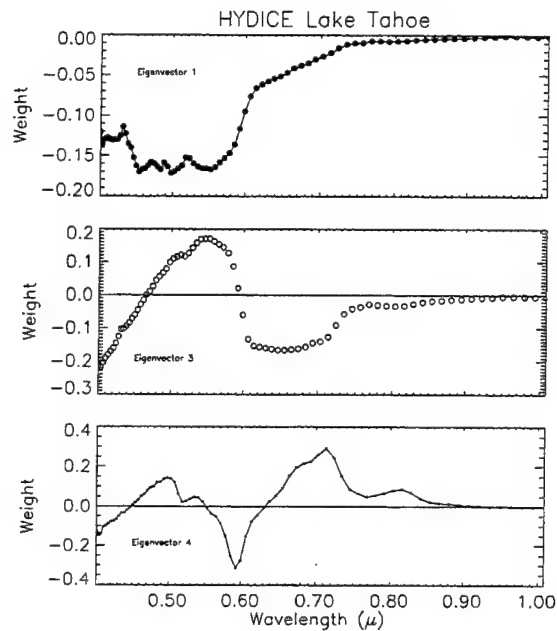


Figure 6.6. Relative weighting of the wavelength dependent data for a few of the first PC-bands. (Bands 1,3 & 4)

The first band, eigenvector 1, is simply a weighted average of the data - roughly the total radiance. Bands 3 and 4 include differences which highlight different scene elements.

1. Constructing Mask for Sandy Bottom Areas

Figure 6.7 is an image of the first PC band which allows easy distinction of shallow water sand and shallow water rock. From this distinction, a mask of the shallow water sand is constructed, Figure 6.8.

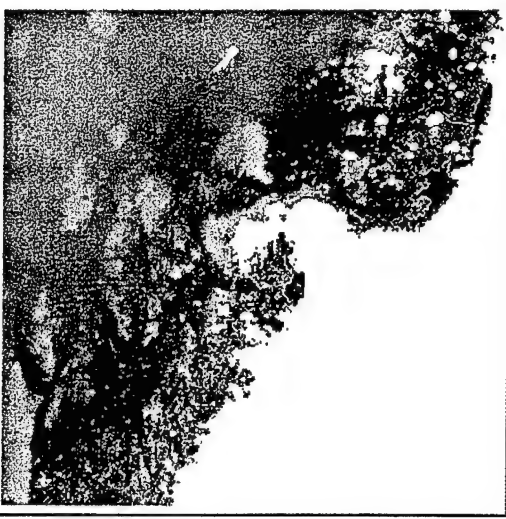


Figure 6.7. PC Band 1 figure, showing contrast between shallow water sand and rock

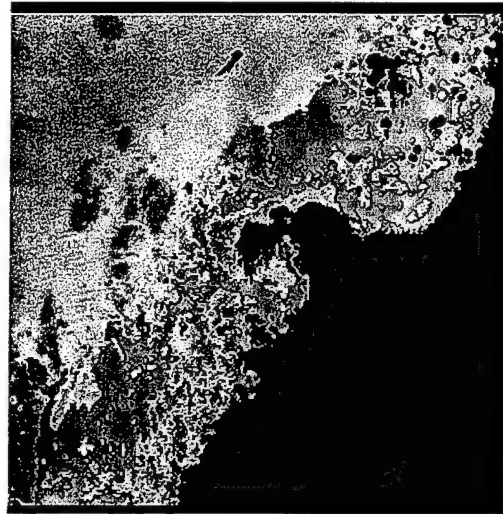


Figure 6.8. Masked shallow water sand in Lake Tahoe scene.

In PC band 4, displayed in Figure 6.9, deep water sand is the prominent feature and is contrasted from the surrounding rocks. A mask can be constructed and added to that of the shallow water for a total sand mask, Figure 6.10.

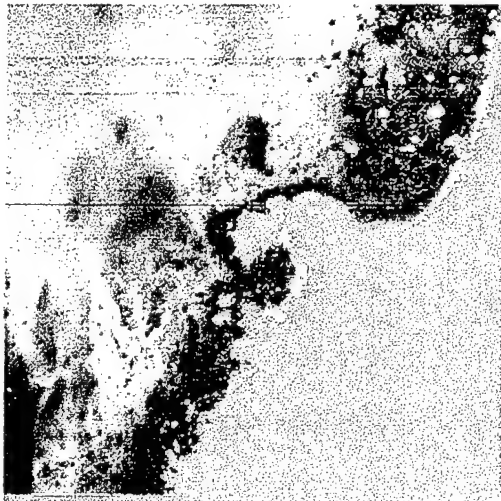


Figure 6.9. PC Band 4, highlighting deep water sand and rock contrasts.

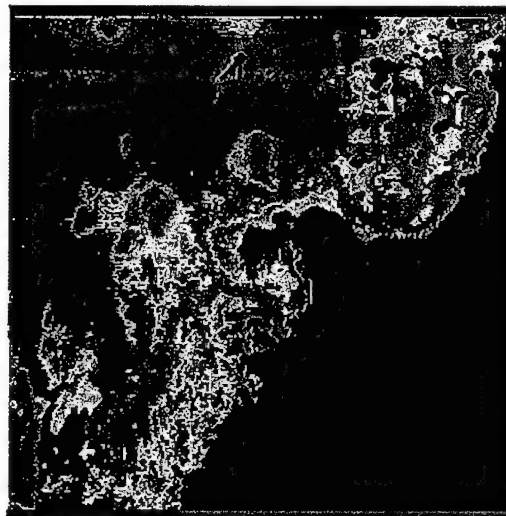


Figure 6.10. Total sand mask in Lake Tahoe scene.

2. Constructing Masks for Dark Areas

Thus far, it has been assumed that the dark areas, within the water scene, were rocks, however, there are two distinct dark areas as characterized by their different radiance spectrum, Figure 6.11.

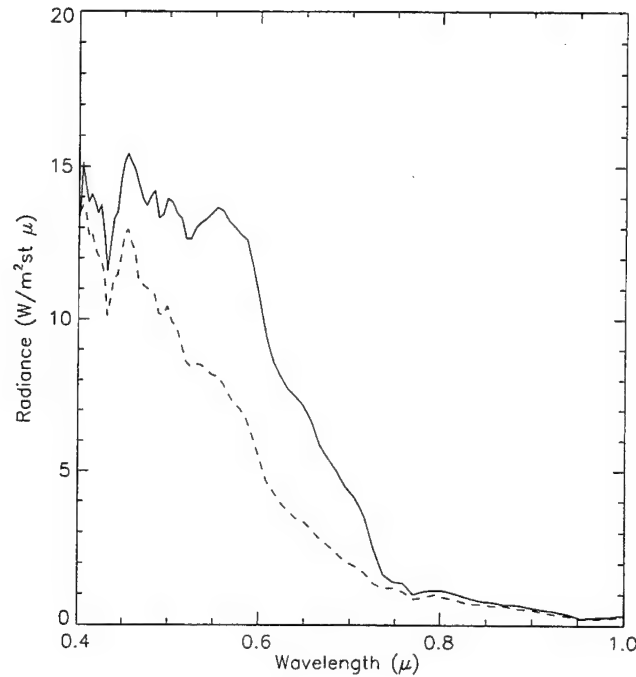


Figure 6.11. Contrasting Spectra from dark bottom material.

The solid line represents the spectra from the brighter of the two material. The difference in the spectra suggest that, if the two material are both rocks, then they are undoubtedly covered by different material. In fact, this is what will be assumed for the remainder of the paper and the two materials will simply be characterized as “bright rock” and “dark rock”.

Taking advantage of the large difference in the radiance around 550 nm, a mask can be constructed for the two different types of rocks within the scene, Figure 6.12a and 6.12.b. This is done by removing all the data within the scene except for that of bright and dark rocks, by applying the mask for sand.



(6.12.a.)



(6.12.b.)

Figure 6.12. Mask for Bright and Dark rocks, (6.12.a and 6.12.b respectively) within the HYDICE Lake Tahoe scene.

The white areas in the scene are the resultant mask for each type of rock.

3. Composite of the Bottom Types

Table 6.1 is a summation of the threshold values and bands used to determine the different masks.

Table 6.1. Threshold values used to define different masks.

Mask	Min Threshold	Max Threshold	Band
Shallow Sand	-13000.0	-3800.0	PC band 1
Deep Sand	5.0	2500.0	PC band 4
Bright Rock	1000.0	10000.0	Water-Sand Masked cube - band 36
Dark Rock	.5	999.0	Water-Sand Masked cube - band 36

As a result of the different mask formation, the Lake Tahoe scene now becomes a composite of three different bottom types; sand - bright rock - dark rock, Figure 6.13.

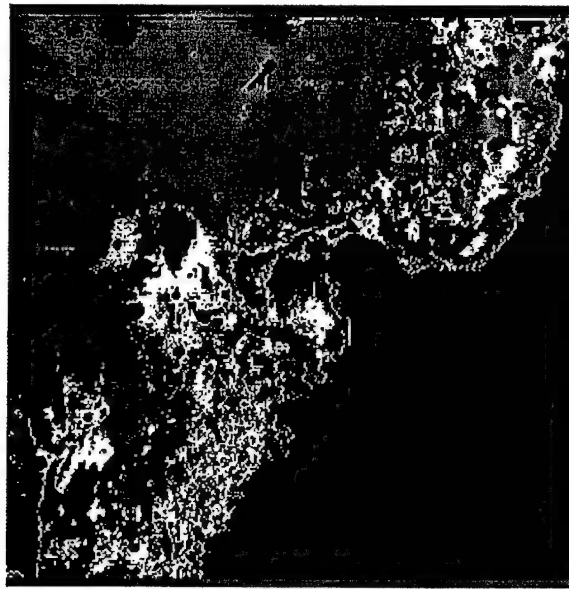


Figure 6.13. Composite of sand and rock masks. (blue - sand, yellow - bright rock, red - dark rock).

The construction of masks for each of these types of bottoms allows for an individual analysis of each bottom type and then a reconstruction of the scene.

B. MODELING DEPTH BY INCLUDING SUBSTRATE REFLECTANCE

Now that the different areas within the scene can be characterized by the reflectance of the underlying substrate, the method of Bierwirth et al. (1993), presented in Chapter III, can again be applied to the Lake Tahoe data. However, including effects of the substrate reflectance, Equation [3.26] will be utilized instead of Equation [3.27].

1. Estimating Substrate Reflectance

The process of characterizing the different substrates, was essentially an exercise in grouping pixels of similar spectra. Once this is done, depth information can be derived by taking advantage of the variability within each of these different substrates classifications. To proceed with the application of Equation [3.26] an estimate must be made for what Bierwirth et al. (1993) refers to as the radiance of wet substrate material for no water cover (L_s described in Chapter III.). Ideally this spectra would be determined at a depth of zero where the substrate is wet but not covered with water. However, in the absence of an exact measurement of the spectra from each of the wet substrates, an approximation can be made by taking near shore-values.

a. Rock Substrate

The areas within the scene that have been characterized as rock, both the bright and dark, have smaller radiance values near-shore than in deeper water. This effect is due to the dark material of the rocks reflecting little radiation, similar to a blackbody. At shallow depths this dark material will resemble a blackbody more closely than when the material is covered by a deeper layer of water (i. e. The bulk water reflectance will add to the water leaving radiance over dark areas of the scene). Consequently, the darkest pixels needed to be determined in order to obtain a characteristic spectra. A histogram of the radiance values from the masked scene can be generated (Figure 6.14 and Figure 6.15) and, from the values within the minimum bin the pixel with minimum spectra can be located and averaged. This was done for both the bright rock and the dark rock, by making use of the masks discussed in the previous chapter. For the bright rock approximately 5 pixels associated with a brightness level of around 1050 were selected. For dark rock approximately 6 pixels associated with a brightness level of around 750 were selected.

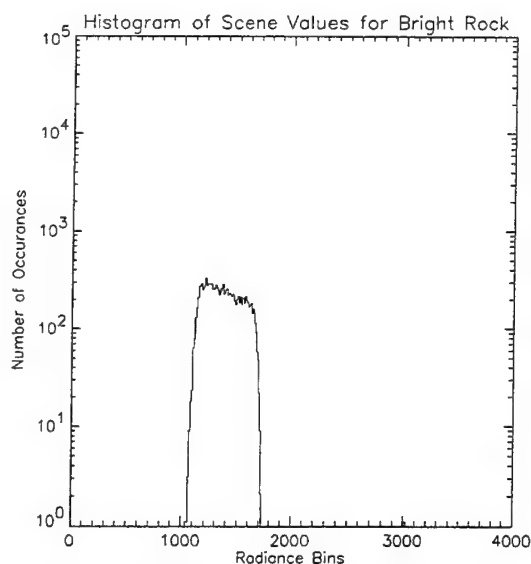


Figure 6.14. Histogram plot for determining shallow water spectra for bright rock within the masked Lake Tahoe data cube.

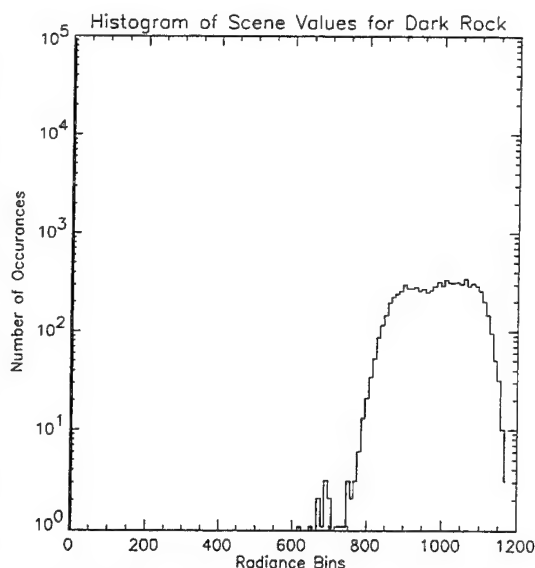


Figure 6.15. Histogram plot for determining shallow water spectra for dark rock within the masked Lake Tahoe data cube.

Notice the difference in radiance values between the bright and dark rock, reiterating the need to treat the two as different types of substrate. The resulting spectra are presented below.

b. Sandy Substrate

In contrast to the dark areas in the scene, the area that has been characterized as sand has large near-shore radiance values that decrease with increasing depth. Therefore, the best estimate of the wet sand spectra is to determine the average of several pixels with the highest spectra. This was again accomplished by plotting a histogram of the radiance values as in Figure 6.16. For sand approximately 7 pixels with brightness values on the order of 3100 were selected and averaged.

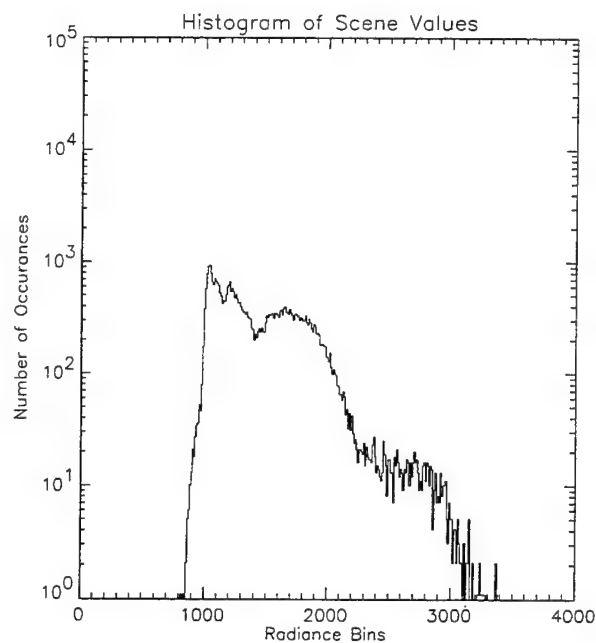


Figure 6.16. Histogram plot for determining shallow water spectra for sand within the masked Lake Tahoe data cube.

c. *Wet Substrate Reflectance*

The wet substrate radiance's are plotted in Figures 6.17.a, 6.17.b and 6.17.c for wet sand, wet bright rock and wet dark rock respectively.

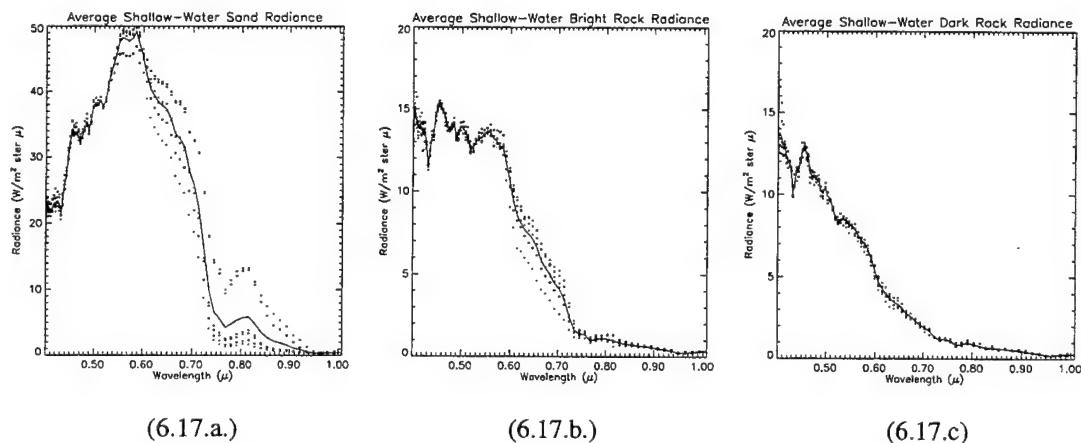


Figure 6.17. Average spectra of wet sand (a), bright rock (b) and dark rock (c).

The solid line in each Figure represents the average of the various dotted spectra. Notice that the bright and dark rock have similar values from about .4 - .5 μm , but differ dramatically from about .5 - .6 μm .

In all cases the pixels used to determine the substrate reflectance were located near the shoreline. This is the expected result as the water will be the shallowest near the shore for each substrate type. Although these values may not be exact for wet substrate with zero water cover, they are probably as close as you can get without making ground truth measurements of each substrate.

2. Depth Results

a. Depth by Using Bottom Reflectance Compared to Depth Without Using Bottom Reflectance

Including the results of substrate reflectance the depth of water in the same three pixels used in Chapter V can now be calculated and compared to the results of Section V.A.3.b.

Table 6.2. Comparison of depth derived without substrate reflectance and with substrate reflectance.

Data Point	Depth without R_s	Depth with R_s
Shallow Water	23.8 m	3.2 m
Deep Water	26.9 m	6.2 m
Rocky Area	29.6 m	1.9 m

As would be expected, a relative decrease in depth between the deep water and the rocky substrate is now observed. Previous results incorrectly showed depth to be larger over the rocky substrate than over deep water. In addition, there is no longer an inherent depth error Δz as was in the previous calculated depth. These results clearly indicate that to

correctly derive depth, the bottom reflectance characteristics must be included in the calculation.

b. Using Substrate Reflectance to Calculate Depth for Entire Scene

Equation [2.26] can now be used to compute the depth at each pixel within the scene. The results of this computation are displayed as Figure 6.18. Figure 6.19 is the published charted depth for Secret Harbor and is provided as a comparison to the calculated depth.

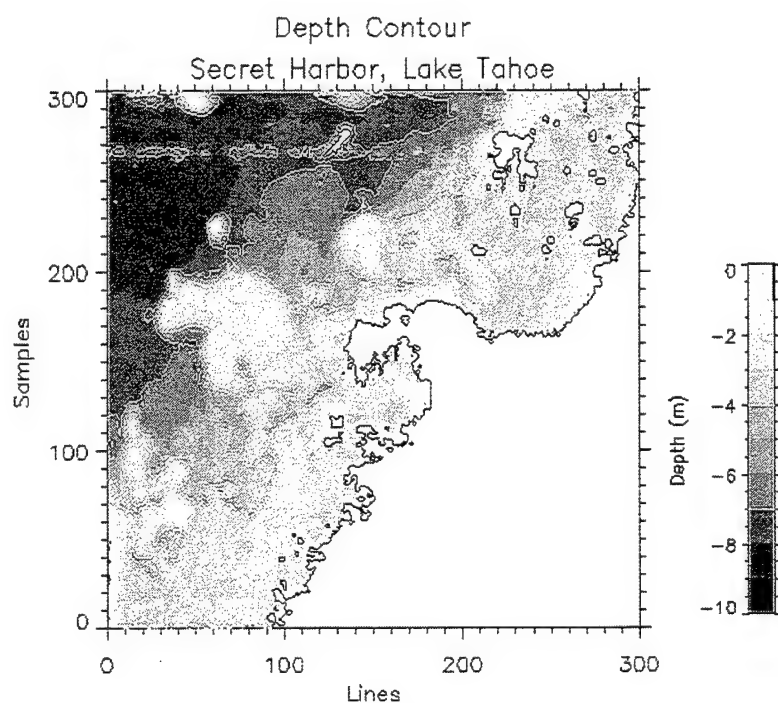


Figure 6.18. Contour plot of derived bathymetry (including effects due to bottom reflectance).

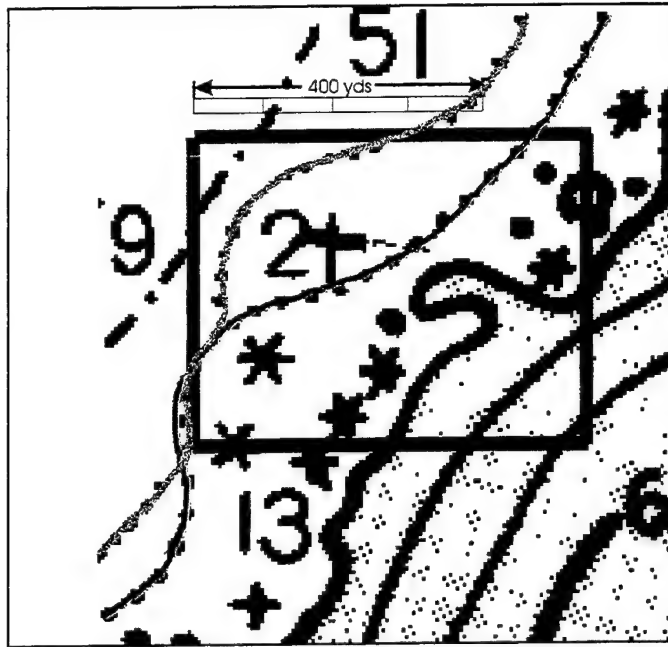


Figure 6.19. Published charted depth. From NOAA (1987).

The dark box in Figure 6.19 is roughly the same area as in Figure 6.18, however Figure 6.19 is shown on a smaller scale to get a better idea of the relative depth of the different curves. The red depth curve (or the bottom curve) in Figure 6.19 is around 4 m. and the yellow curve (or the top curve) is around 7 m. Similarly in Figure 6.18 the 4 m and 7 m curves are highlighted by a white outline. The depth in Figure 6.19 decreases in accordance with the scaling bar to the right of the Figure.

C. RELIABILITY OF ATTENUATION COEFFICIENTS

Much of the dependence on accurate depth derivations is dependent on how well K_d is modeled. Without accurate ground truth measurements for chlorophyll concentrations, K_d was the most worrisome parameter used in the calculations. For that reason, a brief error analysis was completed on how much a variation in chlorophyll will effect the depth calculations. The dynamic chlorophyll range for Lake Tahoe was reported in Kappus et al. to be $.16 \text{ mg m}^{-3}$ at the surface varying to $.26 \text{ mg m}^{-3}$ at 35 m.

Therefore, HYDROLIGHT3.0 was run once for chlorophyll = $.16 \text{ mg m}^{-3}$ and once for chlorophyll = $.26 \text{ mg m}^{-3}$. The depth was then calculated for the entire scene for each set of K_d values resulting in two separate depth scenes. The difference in the depth results for these two scenes is displayed in Figure 6.20.

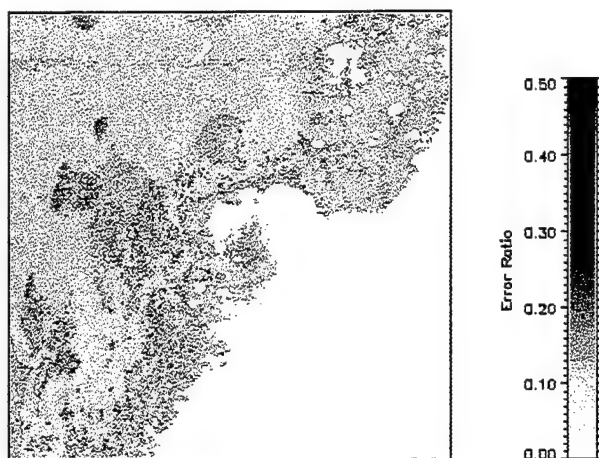


Figure 6.20. Variations in depth due to variations in K_d values.

As can be seen from the scaling bar to the right, the error averages around 10% or so and goes no higher than 50%. This indicates that the assumption of a relatively uniform chlorophyll concentration made earlier will result in only a mild error of depth estimation. It is pointed out that the highest errors in the depth calculations result in areas that were estimated to be bright rock. This leads the author to believe that these areas are in fact rocky substrate that is covered with various amounts of algae. The chlorophyll concentrations within the algae then give rise to the higher depth estimation error reported in Figure 6.20.

VII. SUMMARY AND CONCLUSIONS

High altitude, clear water and low chlorophyll concentrations made Lake Tahoe an ideal spot to begin to develop a method for deriving shallow water bathymetry from hyperspectral data. The scene of Secret Harbor on the eastern shore of the lake provided a clearly varying substrate type and bottom depth that proved to be a good test case for deriving bottom depth. However, given the relatively poor published soundings for the scene, it is difficult to fully assess how close the depth derivations correspond to actual depth. The full data set taken by HYDICE on June 22nd includes the western shoreline just south of Dollar Point, which has been charted in much greater detail. It would be of interest to apply the methods developed in this thesis to this area of the lake to get a better estimation of error.

Atmospheric conditions were modeled by inputting relevant parameters into the radiative transfer model MODTRAN3.5. Similar methods to that of Kappus et al. (1996) were used to correct for atmospheric effects with similar results. The clear, virtually aerosol free conditions, as described in Kappus et al., allowed for a relatively straightforward modeling of the atmosphere above Lake Tahoe the day of the experiment. As a result the derivation of water leaving radiance, L_w , was accomplished with excellent results. A marine boundary layer will introduce a larger, and more difficult to account for, error.

The clear water of Lake Tahoe was assumed to be relatively homogeneous for the purpose of the calculations in this thesis. Ground truth measurements revealed these values to vary between $.16 \text{ mg m}^{-3}$ and $.26 \text{ mg m}^{-3}$ resulting in an average error of about 10% across the scene for that difference in range. The assumption of a relative homogeneous chlorophyll concentration should therefore result in an average error of less than 10% in depth. HYDROLIGHT3.0 was able to adequately model the values for attenuation coefficient K_d given the clear water environment. However, as attempts are made to model water with much higher concentrations of particulate matter, it will

become increasingly more difficult to model, and closer attention will need to be given to thorough ground truth measurements.

As an initial test of the performance of the depth derivation method stated in Bierwirth (1993), the radiance spectra from three separate pixels were analyzed. One of these pixels was located in shallow water over a sandy substrate, one in deep water over a sandy substrate and one over a rocky substrate in relatively shallow water. Calculations resulted in a depth over the three different areas of interest resulted in an erroneous report of depth over the dark rocky substrate with respect to the sandy substrate. In addition, each calculation resulted in a large offset error in actual depth. For these reasons, it was surmised that substrate effects would need to be included to correctly calculate depth. This process has not been included in previous depth derivation methods.

To calculate depth based on substrate type, the scene needed to be divided into different regions. A principle component analysis resulted in the classification of regions of sandy substrate. Once these regions were masked off, the areas of dark and bright rock were differentiated based on spectral differences in selected wave bands. This process was easily completed due to the wide selection of spectral characteristics available from hyperspectral data. A mask for each of the three regions was created.

No ground truth data were available on the spectral characteristics of the three defined substrates. Therefore, a simple program was developed to select and average the most significant near shore values for each bottom type. For sand, the maximum spectral values were chosen and for both types of rock the minimum spectral values were chosen.

Depth was determined for each masked region separately using the respective values of bottom reflectance. The three scenes were then added to form one composite depth contour. Very good agreement was observed between the derived depth contour plot and the published contour plot.

As a result of the analysis of this thesis, it is concluded that it is possible to derive a detailed map of bottom depth from remotely sensed hyperspectral data. This is accomplished by the fact that bottom types are distinguishable from one another based on

variations within the hyperspectral data. By developing similar techniques to survey turbid coastal waters, information can be provided to the war fighter concerning a targeted coastal landing zone. This can be accomplished with limited risk to human life and military equipment.

LIST OF REFERENCES

- Anon, "Underwater Depth Determination", *Photographic Interpretation Handbook, Supplement No. 18*, Photographic Intelligence Center, Division of Naval Intelligence, Navy Department., 1945.
- Berk, A., Bernstein, L. S., Robetson, D. C., Acharya, P. K., Anderson, G. P., Chetwynd, J. H., "MODTRAN Cloud and Multiple Scattering Upgrades with Application to AVIRIS", *Preliminary Summaries of the 6th Annual JPL Airborne Earth Science Workshop*, March 4-8, Vol 1. AVIRIS Workshop, Ed. R. O. Green, JPL, Pasadena CA, 1996.
- Bierwirth, P. N., Lee, T. J., Burne, R. V., "Shallow Sea-Floor Reflectance and Water Depth Derived by Unmixing Multispectral Imagery", *Photogrammetric Engineering & Remote Sensing*. Vol. 59, No. 3, pp. 331-338., March 1993.
- Cassidy, Charles J., "Airborne Laser Mine Detection Systems", September, 1995.
- Collins, Brian H., "Thermal Imagery Spectral Analysis", September, 1996.
- Earth Observation Research Center (EORC), "Advanced Earth Observing Satellite - MIDORI", mentor.eorc.nasda.go.jp/ADEOS/index.html, November, 1996.
- Elachi, Charles, *Introduction to the Physics and Techniques of Remote Sensing*, John Wiley & Sons, Inc., New York, 1987.
- Gaskell, T. F., *World Beneath the Oceans*, The Natural History Press, Garden City, New York, 1964.
- Hamilton, M.K., Davis, C.O., Rhea, W.J., Pilorz, S.H., Kendall, L.C., "Estimating Chlorophyll Content and Bathymetry of Lake Tahoe Using AVIRS Data.", *Remote Sens. Environ.* 44, pp. 217-230, 1993.
- Hyperspectral Masint Support to Military Operations (HYMSMO), *Collection and Exploitation Operations Plan (CEOP)*, 1996.
- Jupp, D.L.B., "Background and Extensions to Depth of Penetration (DOP) Mapping in Shallow Coastal Waters.", *Symposium on Remote Sensing of the Coastal Zone*, Gold Coast, Queensland, Session 4, Paper 2, 1988.
- Kappus, M.E., Davis, C.O., Rhea, W.J., "HYDICE data from Lake Tahoe: comparison to coincident AVIRIS and in-situ measurements.", *Proceedings of the SPIE V. 2819*, August 1996.

Klein, Miles V., Furtak, Thomas E., *OPTICS, Second Edition*, John Wiley & Sons, Inc., New York, 1986.

Kidder, S.Q., Vonder Harr, T.H., *Satellite Meteorology: An Introduction.*, Academic Press, Inc., San Diego, 1995.

Kramer, H. J., *Earth Observation Remote Sensing - Survey of Missions and Sensors.*, Springer-Verlag, Berlin, 1992.

Lyzenga, D.R., "Shallow-water bathymetry using combined lidar and passive multispectral scanner data.", *INT. J. Remote Sensing*, Vol. 6, No.1, pp. 115-125, 1985.

Lyzenga, D.R., "Passive remote sensing techniques for mapping water depth and bottom features.", *Applied Optics*, Volume 17, No. 3., pp. 379-383, 1978.

McCurdy P. G., *Manual of Aerial Photogrammetry: Application of Aerial Photogrammetry in the Compilation of Hydrographic Charts*, H. O. Pub. No. 591, Reprinted, June 1946, H. O. Misc. No. 9257, 1940.

Mobley, C.D., *Light and Water: Radiative Transfer in Natural Waters*, Academic Press, Inc., San Diego, 1994.

Mobley, C. D., *HYDROLIGHT 3.0 Users' Guide*, SRI International, 1995.

NASA, *Oceanography From Space Portfolio*, U. S. Government Printing Office, 1986-680-616, 1986.

NOAA, *Chart Number 18665*, U. S. Department of Commerce, National Oceanic and Atmospheric Administration, National Ocean Service, Washington D. C., January 1987.

Pickard, G.L., Emery, W.J., *Descriptive Physical Oceanography: An Introduction.*, Pergamon Press, Inc., New York, 1990.

Polcyn, F. C., Brown, W. L., Sattinger, I. J., "The Measurement of Water Depth by Remote Sensing Techniques", *Report 8973-26-F*, Willow Run Laboratories, The University of Michigan, Ann Arbor, 1970.

Robinson, M.A., *Satellite Oceanography: An introduction for oceanographers and remote-sensing scientists*, Ellis Horwood Limited, Chichester, England, 1985.

Sandwell, D. T., Smith, W. H. F., 'Exploring the Ocean Basins with Satellite Altimeter Data', www.ngdc.noaa.gov/mgg/announcements/text_predict.HTML, November 1995.

Stewart, R.H., *Methods of Satellite Oceanography*, University of California Press, Berkeley and Los Angeles, 1985.

INITIAL DISTRIBUTION LIST

1. Defense Technical Information Center 2
8725 John J. Kingman Road., STE 0944
Ft. Belvoir, VA 22060-6218

2. Dudley Knox Library 2
Naval Postgraduate School
411 Dyer Rd.
Monterey, CA 93943-5101

3. Captain A. Legrow, Navy TENCAP 1
Code N632, Rm. 5D773
The Pentagon
Washington, DC 20350-2000

4. Commander Jelinek, Navy TENCAP 1
Code N632, Rm. 5D773
The Pentagon
Washington, DC 20350-2000

5. Richard C. Olsen, Code PH/OS 5
Department of Physics
Naval Postgraduate School
Monterey, CA 93943-5002

6. Newell Garfield, Code OC/GF 2
Department of Oceanography
Naval Postgraduate School
Monterey, CA 93943-5002

7. Greg Pavlin, SITAC 1
11781 Lee Jackson Mem. Hwy.
Suite 500
Fairfax, VA 22033-3309

8. Mark Anderson, SITAC 1
11781 Lee Jackson Mem. Hwy.
Suite 500
Fairfax, VA 22033-3309

9. Ron Resmini, SITAC 1
11781 Lee Jackson Mem. Hwy.
Suite 500
Fairfax, VA 22033-3309
10. Curt Davis, NRL 1
Remote Sensing Division, Code 72xx
4555 Overlook Ave., SW
Washington, DC 20375
11. Mary Kappus, NRL 1
Remote Sensing Division, Code 7210
4555 Overlook Ave., SW
Washington, DC 20375
12. LT Doug Stuffle 2
1460 DiBlasi Dr.
Las Vegas, NV 89119